System-Level Large-Scale Multidisciplinary Design Optimization of an Air Taxi Concept *

Marius L. Ruh[†], Michael A. P. Warner[‡], Luca Scotzniovsky[§], Andrew H. Fletcher [¶], Mark Z. Sperry [‖], and John T. Hwang[**]
University of California San Diego, 9500 Gilman Dr, La Jolla, CA 92093

The rise of urban air mobility as a solution to alleviate congestion in metropolitan areas has spurred the development of novel vertical takeoff and landing aircraft, renewing research interest in conceptual design. Adjoint-based multidisciplinary design optimization naturally suits aircraft design by efficiently searching high-dimensional design spaces. However, solving system-level large-scale aircraft design problems reliably remains challenging due to numerical conditioning issues arising from simultaneously modeling many design conditions and disciplines. This paper presents a novel demonstration of system-level large-scale multidisciplinary design optimization of an urban air mobility concept using an integrated, physics-based computational model. We solve a gross weight minimization problem of a lift-plus-cruise reference vehicle with 161 design variables and 96 constraints across 15 design conditions, representing nominal mission and failure conditions. Our computational model integrates physics-based models for aerodynamics, propulsion, structures, aeroacoustics, motor performance, and static stability. The optimized design achieves a 6.5% reduction in gross weight. Parameter sweeps over battery energy density and end-of-mission state of charge confirm the robustness of our approach. Using standard computational resources, the average time for solving the large-scale problem is 1.6 hours. These findings highlight the potential of large-scale multidisciplinary design optimization in accelerating aircraft conceptual design.

Nomenclature

Acronyms

UAM	=	urban air mobility

*Parts of this paper were originally presented at the *AIAA SCITECH 2024 FORUM* held January 8-12, 2024 in Orlando, Fl. Paper number: AIAA 2024-0771 https://doi.org/10.2514/6.2024-0771

[†]PhD Candidate, Department of Mechanical and Aerospace Engineering, AIAA student member, mruh@ucsd.edu
[‡]PhD Student, Department of Mechanical and Aerospace Engineering, AIAA student member
[§]PhD Student, Department of Mechanical and Aerospace Engineering, AIAA student member
[¶]PhD Student, Department of Mechanical and Aerospace Engineering, AIAA student member
[‖]PhD Candidate, Department of Mechanical and Aerospace Engineering, AIAA student member
[**]Associate Professor, Department of Mechanical and Aerospace Engineering, AIAA senior member

eVTOL	=	electric vertical takeoff and landing
MDO	=	multidisciplinary design optimization
FFD	=	free-form deformation
VLM	=	vortex lattice method
BEM(T)	=	blade element momentum (theory)
DI	=	dynamic inflow
EB	=	Euler–Bernoulli
ECM	=	equivalent circuit model
SPL	=	sound pressure level
OEI	=	one engine inoperative
SoC	=	state of charge
(X)DSM	=	(extended) design structure matrix
CADDEE	=	comprehensive analysis and high-dimensional design environment for engineering systems
SIFR	=	solver-independent field representation
CSDL	=	computational system design language

Symbols

α	=	angle of attack
Re	=	Reynolds number
Ma	=	Mach number
ρ	=	air density
$\boldsymbol{\Gamma_b}$	=	vector of bound vortex circulation strengths
$\boldsymbol{A}$	=	aerodynamic influence coefficients matrix
$\boldsymbol{v}$	=	undisturbed flow velocity
$\boldsymbol{n}$	=	vortex panel normal vector
V_x	=	free-stream velocity
V_θ	=	rotational velocity
u_x	=	total axial-induced velocity at the rotor disk
u_θ	=	azimuthally induced velocity
W	=	resultant inflow velocity
r	=	radial distance from rotor hub
c	=	sectional chord length

$\bar{r}$	=	normalized radial distance from hub
ϕ	=	sectional rotor inflow angle
C_l	=	2-D airfoil lift coefficient
C_d	=	2-D airfoil drag coefficient
ψ	=	azimuth angle
dT	=	sectional thrust
dQ	=	sectional torque
$\boldsymbol{\lambda}$	=	inflow state vector
$\boldsymbol{M}_{\text{prop}}$	=	mass matrix for dynamic inflow model
$\boldsymbol{L}$	=	derivative matrix for dynamic inflow model
$\boldsymbol{c}$	=	vector of aerodynamic loading coefficients C_T, C_L, C_M
C_T	=	rotor thrust coefficient
C_L, C_M	=	rotor moment coefficients
$\boldsymbol{K}$	=	global stiffness matrix
$\boldsymbol{u}_{\text{nodal}}$	=	vector of nodal displacements
$\boldsymbol{f}_{\text{nodal}}$	=	vector of nodal forces and moments
σ'	=	critical plate buckling stress
E	=	Young's modulus
ν	=	Poisson's ratio

I. Introduction

Urban air mobility (UAM) envisions safe, efficient, and affordable transportation of people and goods across metropolitan areas through manned or unmanned aircraft [1]. Key requirements to enable this technology are vertical takeoff and landing (VTOL) capabilities, a low carbon footprint, high safety standards, and low noise emissions. Existing air and rotorcraft do not meet these requirements, which has led to the development of over 1000 new VTOL concepts as of April 2024, according to the Vertical Flight Society*. Most of these concepts combine the aerodynamic efficiency of fixed-wing aircraft with the VTOL capabilities of helicopters to address the challenges of UAM operations. There are various configurations, and no proposed concept has proven to be a clear front-runner. This, in part, has renewed interest in advancing aircraft conceptual design methods to quickly evaluate the potential of different UAM concepts.

Traditional conceptual design approaches [2–4] typically make use of regressions, semi-empirical, or low-fidelity physics-based models. There exist several well-established software frameworks that are built around these low-order

*https://vtol.org/news/press-release-vfs-electric-vtol-directory-hits-1-000-designs methods such as NASA's Flight Optimization System (FLOPS) [5], the Common Parametric Aircraft Configuration Scheme (CPACS) [6] by the German Aerospace Center (DLR), and NASA's Design and Analysis of Rotorcraft (NDARC) [7] framework. These research codes provide fast evaluation times and reasonable accuracy for conventional aircraft and rotorcraft configurations due to an abundance of historically available data and well-understood interactions between disciplines and subsystems. However, since UAM aircraft are a new class of aircraft with novel configurations and unique mission requirements, conventional aircraft design approaches may not lead to interpretable results that account for complex interactions between subsystems (e.g., powertrain and airframe) as well as between disciplines (e.g., aerodynamics and structures) with acceptable accuracy.

There has been high research activity in many areas surrounding the conceptual design of novel UAM aircraft in recent years. Areas of active research include a) analysis and sizing of novel (hybrid)-electric propulsion architectures [8–15], b) trajectory optimization [16–23], c) aeroacoustic analysis and optimization [24–31], d) rotor-rotor and rotor-wing interactions[32–38], e) structural analysis and weight estimation [39–44], f) fast vehicle sizing and conceptual design [45–50], g) large-scale multidisciplinary design optimization using adjoint-based sensitivity analysis [51–56], and h) software and modeling frameworks [57–61]. Many of these studies make use of low-to-medium-fidelity models or create parametric or data-driven models from high-fidelity data. In addition, many studies focus explicitly on high-fidelity simulations, e.g., in the field of aeroacoustics [62] or aerodynamics [63]. However, at the conceptual level, the computational cost of high-fidelity simulations quickly becomes prohibitive as more disciplines and design conditions (i.e., vehicle sizing conditions) are included.

For comprehensive system-level aircraft conceptual design, large-scale multidisciplinary design optimization (MDO) is an attractive option due to its efficiency in searching a high-dimensional design space to find an optimal design. Here, "large-scale" refers to problems with 100–1000s of design variables, and "comprehensive system-level" implies that the computational model takes into account many design conditions and all major subsystems and disciplines. For problems of this magnitude, using gradient-based algorithms is often the only feasible option due to their efficiency compared to gradient-free algorithms (see e.g., [64]). State-of-the-art MDO frameworks like NASA's OpenMDAO [65] allow for the construction of complex computational models and efficient computation of total derivatives using the unified derivatives equation [66]. A limitation of OpenMDAO is that it does not automate the computation of analytic partial derivatives. For most large-scale problems, the use of the finite difference derivative approximation is impractical due to round-off and truncation errors and additional required model evaluations. The manual implementation of analytical derivatives significantly increases the implementation effort, especially for physics-based models, which typically involve nonlinear residual equations.

Recent advances in automated adjoint-based sensitivity analysis [67] have enabled the application of large-scale MDO to the conceptual design of novel aircraft using low-fidelity physics-based models and a small set of design conditions (see e.g., [51]). However, there exists a research gap in terms of problem complexity and modeling fidelity.

For comprehensive system-level design, it is necessary to consider more design conditions , such as transition maneuvers and subsystem failure conditions like one-engine-inoperative (OEI) or structural sizing conditions. This requires the use of more advanced predictive models, e.g., ones that can adequately model rotors in edgewise flight. Solving MDO problems of this complexity in a reliable manner is challenging due to numerical conditioning issues that arise from poor design variable scaling and bad initial guesses, causing optimization algorithms to fail. Achieving favorable scaling and initial guesses is difficult as design variables may span several orders of magnitude given certain choices of units (e.g., flight distances versus structural skin thicknesses), and feasibility constraints are often highly nonlinear.

In this paper, we present a novel demonstration of comprehensive, system-level large-scale MDO of a lift-plus-cruise UAM reference vehicle. The novelty lies in the breadth of our computational model, which spans all major subsystems and disciplines, and in the simultaneous consideration of a large number of design conditions. Specifically, we consider 15 distinct design conditions, including a nominal mission composed of hover, a quasi-steady transition maneuver, climb, cruise, and descent, as well as four OEI conditions and two static structural sizing conditions. The computational model integrates several low to mid-fidelity physics-based and regression models: the vortex lattice method (VLM), blade element momentum (BEM) theory, a rotor dynamic inflow model, an Euler–Bernoulli beam model, weight regressions, aeroacoustic models for tonal and broadband noise, an equivalent circuit model (ECM) for motor performance, an energy-based battery model, and aircraft trim and static stability analysis. We solve a gross weight minimization problem with 161 design variables and 96 constraints. Two key factors enable us to reliably solve this large-scale MDO problem: first, a newly developed graph-based modeling language that fully automates adjoint-based sensitivity analysis; and second, a multi-stage optimization strategy, in which we solve four smaller suboptimization problems to generate a good initial guess and appropriate design variable scaling for the full-scale problem. We demonstrate the robustness of our approach by conducting parameter sweeps comprised of 20 distinct optimization problems, in which we vary constant parameters of the computational model (battery energy density and end-of-mission state of charge).

The remainder of this paper proceeds as follows. First, we describe our computational approach in Sec. II, including our approach for automated sensitivity analysis in Sec. II.A, geometry parameterization in Sec. II.B, and optimization framework in Sec. II.E. Next, in Sec. III, we give an overview of the predictive models that we use in this study. Then, we give a brief description of the NASA lift-plus-cruise concept vehicle as the test bed for our design optimization study in Sec. IV. Lastly, we present the results in Sec. V.

II. Computational Approach

In this section, we describe our computational approach, which includes sensitivity analysis (II.A), geometry parameterization (II.B), the assembly of computational models (II.C), constraint aggregation (II.D), the optimization framework (II.E), and the definition of a baseline design (II.F).

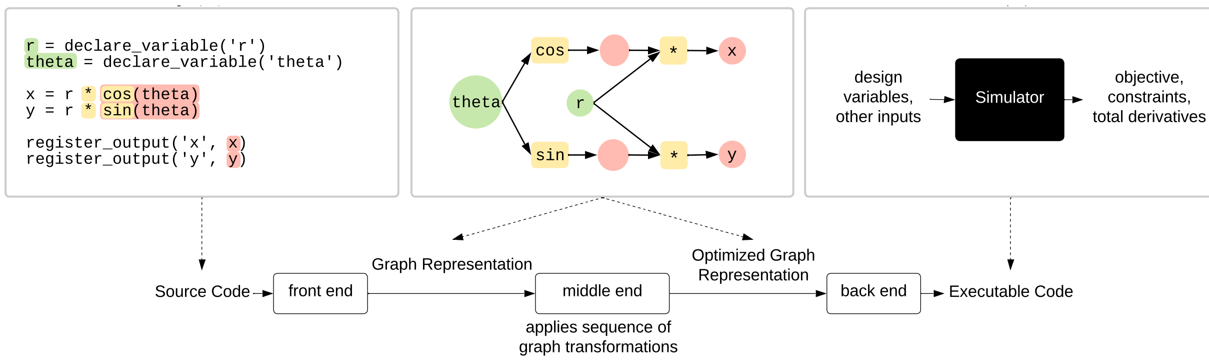

Fig. 1 From Gandarillas et al., a visualization of a CSDL computational graph constructed using its API [67].

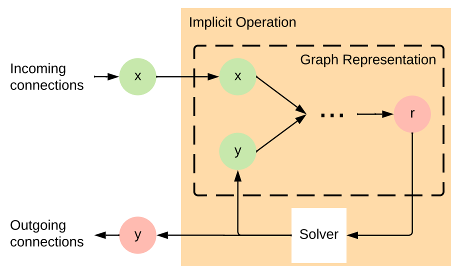

Fig. 2 From Gandarillas et al., a graph representation of an implicit function solved using a nonlinear solver [67].

A. Sensitivity Analysis

The Computational System Design Language (CSDL) [67] is an algebraic modeling language in Python that uses a graph-based approach to construct user-defined computational models as seen in Fig. 1. CSDL provides a Pythonic interface similar to NumPy, allowing users to easily construct complex MDO models. It also provides an interface to build implicitly defined functions commonly used in MDO problems, which are evaluated using nonlinear solvers.

CSDL constructs a directed, acyclic computational graph of the model, storing dependencies between variables and mathematical operators. This graph data structure is used to accelerate the model evaluation time and automatically compute optimization derivatives. The model acceleration is achieved by translating the model to a JAX [68] computational backend, where JAX is a Google-supported Python library that enables fast execution of Python code. Automatic derivative computation of dependent variables with respect to independent variables is done by applying reverse-mode differentiation to the graph [69], eliminating the need to hand-derive or manually implement model derivatives. Reverse-mode differentiation using vector-Jacobian products also has the added benefit of being computationally efficient when the number of independent variables greatly exceeds the number of dependent variables, and is a technique used in other software [65, 70].

For implicitly defined functions, using standard reverse-mode differentiation to evaluate derivatives can be expensive as it involves propagating derivatives backwards through multiple nonlinear solver iterations. CSDL overcomes this issue by leveraging the implicit function theorem. Consider a continuously differentiable function $F(x, y) : \mathbb{R}^{n+m} \to \mathbb{R}^m$ where $y \in \mathbb{R}^m$ contains the dependent variables and $x \in \mathbb{R}^n$ contains the independent variables. A representation of this in a graph is shown in Fig. 2. At a point (x^*, y^*) where $F(x^*, y^*) = 0$, the implicit function theorem states

$$\frac{\partial y}{\partial x}(x^*, y^*) = -F_y(x^*, y^*)^{-1} F_x(x^*, y^*), \tag{1}$$

where F_x and F_y denote the partial derivative Jacobians of F with respect to x and y.

This can be leveraged for reverse-mode differentiation. Specifically, the vector-Jacobian product of x, $\bar{x}$, is solved for using

$$F_y(x^*, y^*)^T \Psi^T = \bar{y}^T, \quad \bar{x} = -\Psi F_x(x^*, y^*), \tag{2}$$

where $\bar{y}$ is the vector-Jacobian product of y [69]. This process requires only a single linear system solve at the fixed point, which is independent of the number of nonlinear solver iterations. We note that this approach of applying reverse-mode differentiation using vector-Jacobian products is also known as the adjoint method, and Ψ is often referred to as the adjoint vector. CSDL's automated computation of analytic sensitivities for implicit operations offers a key advantage, as many discipline models (see Sec. III) involve implicitly defined nonlinear residuals. This significantly reduces the implementation effort for implicit sensitivity analysis.

B. Geometry Parameterization

The central geometry is a high-fidelity representation from which discretizations (i.e., meshes) needed for each physics-based solver can be derived. We use B-spline surfaces, which are widely used for representing complex geometries [71]. Solver-specific meshes are computed as a function of the control points of the central geometry. As such, when the geometry control points are manipulated by the geometry parameterization, the meshes are easily reevaluated to be consistent with the updated geometry. An example of a central geometry representation is shown in Fig. 3a for a lift-plus-cruise eVTOL concept with overlaid meshes for aerodynamic analysis (vortex lattice method) and structural analysis (beam).

The geometry is parameterized using a sequence of steps, shown in Fig. 4. First, the geometry control points of each component, (e.g., wing), are parameterized using the free form deformation (FFD) method. These FFD blocks are then further parameterized using a sectional parameterization, shown in Fig. 3b, which defines sets of control points along a principal axis as sections that can rigidly translate, rigidly rotate, flexibly stretch, or any combination of the three. Furthermore, the sectional parameterization uses a B-spline curve for each sectional parameter. Finally, the entire aforementioned parameterization is used as the forward model for the geometry parameterization solver. We formulate a nested optimization problem and leverage CSDL's computational graph to automatically form and solve the first-order

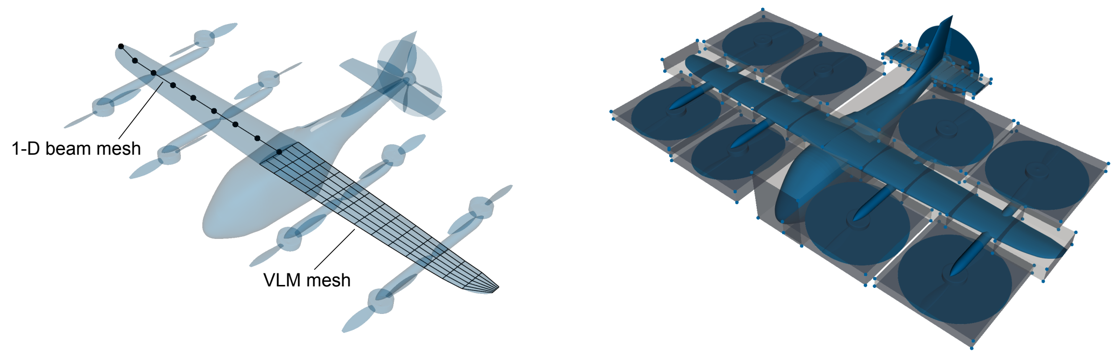

(a) Central geometry representation with overlaid VLM and beam meshes

(b) Central geometry parameterization using FFD blocks and parameterized sections

Fig. 3 Geometry representation and parameterization of a lift-plus-cruise concept

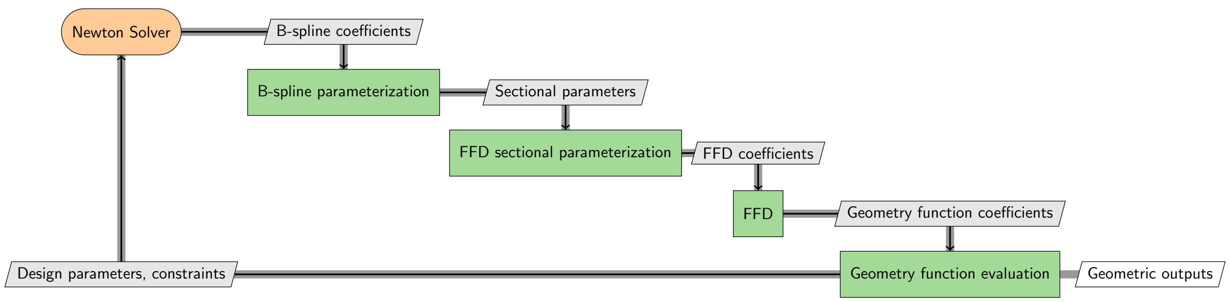

Fig. 4 XDSM of the Geometry Parameterization Solver

optimality conditions, which are used as the residual for a nonlinear Newton solver. The residual is

$$\boldsymbol{R}_{\text{geo}}(\boldsymbol{x}) = \begin{bmatrix} \nabla_x F_{\text{geo}} + \lambda^T \nabla_x C_{\text{geo}} \\ C_{\text{geo}}(\boldsymbol{x}) \end{bmatrix}, \tag{3}$$

where the objective $F_{\text{geo}}(\boldsymbol{x}) = \boldsymbol{x}^T \boldsymbol{W} \boldsymbol{x}$ is the weighted ($\boldsymbol{W}$ is a diagonal matrix of weights) square of the l^2 norm of the B-spline coefficients (i.e. control points) $\boldsymbol{x}$. As such, the geometry parameterization solver computes the set of B-spline control points that will achieve the design specified by the optimization design variables (e.g., wing span) that require the least amount of "energy". For example, to change the wing span, the parameterization solver will only translate the coefficients of the parameterized sections along the principal direction and will not stretch or rotate them, unless other design changes like wing twist or area are desired. The diagonal weight matrix $\boldsymbol{W}$ can restrict certain degrees of freedom by introducing a penalty factor that forces the parameterization solver not to use certain B-spline coefficients to achieve the desired design. Lastly, the constraint function $C_{\text{geo}}(\boldsymbol{x})$ is a mapping from the B-spline control points $\boldsymbol{x}$ to a set of geometric constraints. An example is a kinematic constraint between a rotor boom and a wing. As the wingspan increases, the boom translates accordingly.

C. Assembly of Computational Models

1. Modeling Framework

The discipline models (see Sec. III) are assembled using a newly developed aircraft design framework called the Comprehensive Analysis and high-Dimensional Design Environment for Engineering systems (CADDEE), which has been used in previous studies (see e.g., [51, 52]). A high-level workflow of the CADDEE framework is shown in Fig. 5 as a design structure matrix (DSM). First, the geometry is defined for the base configuration of the aircraft, which includes defining vehicle components and the FFD analysis. Next, the design conditions are defined and parameterized in terms of high-level quantities like range, speed, altitude, etc. Subsequently, the mass properties for the vehicle are defined on a per-component basis and summed to determine the aircraft-level mass properties. In this process, we make use of the parallel axis theorem for computing the total vehicle inertia tensor. Next is the condition analysis. Here, discipline models are evaluated using inputs coming from the geometry, condition, and mass properties blocks. These models are evaluated on a per-design condition basis and usually compute optimization constraints. Lastly, in the post-processing step, outputs from each design condition analysis are assembled to compute quantities of interest that depend on the entire mission profile, e.g., the final battery state of charge.

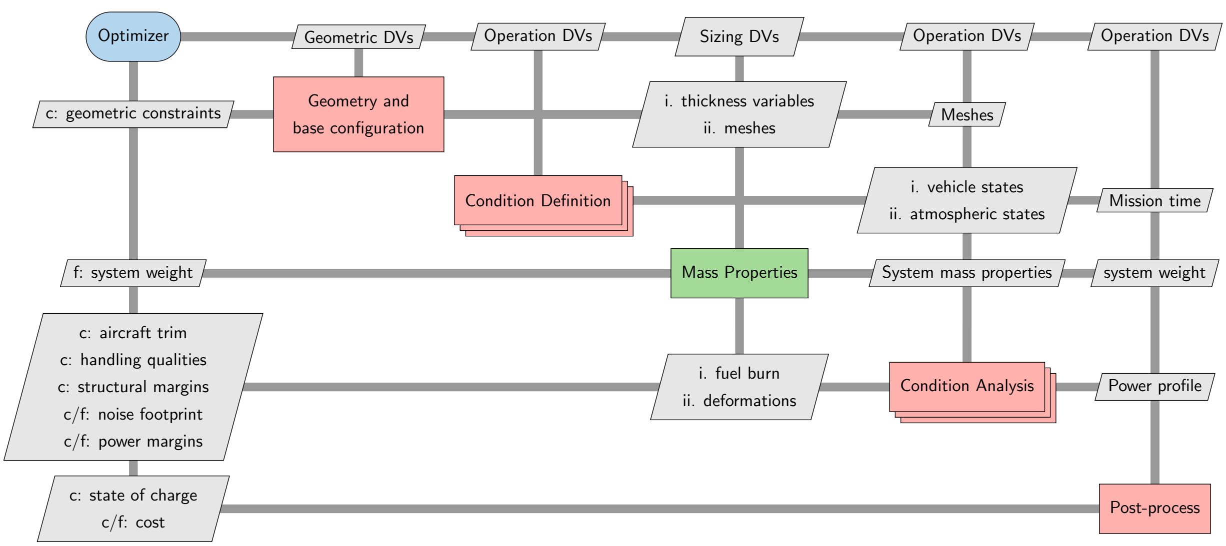

Fig. 5 DSM of the general CADDEE workflow

2. Solver-Independent Field Representation

The Solver Independent Field Representation (SIFR) approach [72], integrated within CADDEE, facilitates interfacing between solvers and distributed data. Building on CADDEE's central geometry representation, SIFR unifies the treatment of all field quantities, including those associated with design variables, solver states, and constraints. This is achieved by representing fields through functions that share a common parametric domain with the geometry.

Just as a geometry function can be evaluated at a parametric coordinate to yield a physical coordinate, the same parametric coordinate can be used to evaluate a pressure function or a displacement function to determine the pressure and displacement at that physical coordinate. This relationship is shown in Fig. 6.

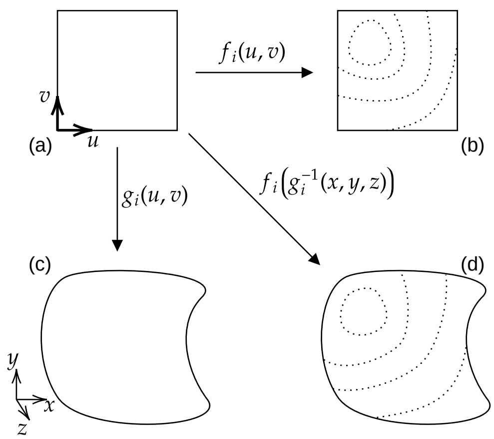

Fig. 6 Parametric mappings for SIFR: (a) parametric space, (b) field in parametric space, (c) geometry in physical space, (d) field on geometry in physical space [72]

In general, SIFR uses functions of the form

$$f(u,v) = \boldsymbol{B}(u,v)\boldsymbol{C} \tag{4}$$

where $\boldsymbol{B}(u,v) \in \mathbb{R}^{N_e \times N_c}$ is a basis matrix that maps between the coefficients that define the function, $\boldsymbol{C} \in \mathbb{R}^{N_c \times 3}$, and the field values at parametric coordinates (u,v). Here, N_e refers to the number of evaluated points and N_c is the number of function coefficients (e.g., control points). Within CADDEE, for example, the geometry is usually represented using B-spline surfaces of the form:

$$g(u,v) = \sum_{i=0}^{m}\sum_{j=0}^{n} B_{i,p}(u)B_{j,q}(v)c_{ij} \tag{5}$$

The degrees p and q of each parametric-coordinate-wise basis function $B_{i,p}(u)$ and $B_{j,q}(v)$ may vary from surface to surface, as can the number of control points n and m. SIFR permits a variety of function spaces in addition to B-splines, such as inverse-distance weighting, polynomial, and piecewise-constant function spaces. Each field may be represented by a different function space mapping from the same parametric coordinates, and different function spaces may even be used for different sub-surfaces of the same field.

These functions play a crucial role in the SIFR approach for modular, conservative state transfer between solvers. Rather than directly linking internal state representations across solvers in different domains, the SIFR framework connects each solver to CADDEE's central field representation. This is done in two steps between three different representations, shown in Figure 7. The first is a mapping between the solver's internal representation of a field to a nodal representation consisting of a set of values at points on the geometry. This mapping is specific to each solver and may be trivial in some cases, such as a shell-based structural model. The second is a mapping from the nodal representation to the framework representation. Specifically, this consists of fitting a function from the chosen function space to the field data contained in the nodal representation. In practice, this is usually a least-squares fit of the coefficients $\boldsymbol{C}$ implemented using a Moore–Penrose pseudoinverse of the matrix $\boldsymbol{B}$ in Eq. (4). The reverse of this process is used to transfer field data from the framework to a solver. The functional representation is evaluated at a set of points on the geometry, resulting in a nodal representation, which is then mapped into the solver's internal representation. This process can be augmented to enforce conservation of invariants such as virtual work in the load and displacement transfer via a modification of the fitting step, as demonstrated by van Schie et al. [73]. Conservation is enforced between each solver and the framework, rather than directly between solvers, maintaining solver modularity. This is accomplished by adding a constraint on the invariant to the fitting step in the data transfer process.

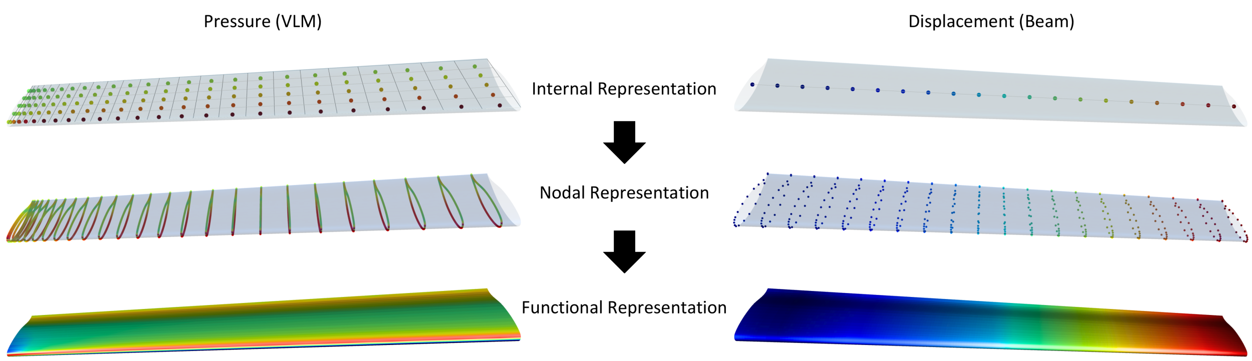

Fig. 7 SIFR process applied to vortex lattice method and beam analysis of wing

Following the SIFR methodology, displacements at nodes on the wing surface are obtained from the beam solution using the Euler–Bernoulli kinematic assumptions [74]:

$$u_x(x, y, z) = u_{x,0}(x) - y\,\frac{\partial u_{y,0}}{\partial x} - z\,\frac{\partial u_{z,0}}{\partial x}, \tag{6a}$$

$$u_y(x, y, z) = u_{y,0}(x), \tag{6b}$$

$$u_z(x, y, z) = u_{z,0}(x), \tag{6c}$$

where (u_x, u_y, u_z) denote the displacement components at a point (x, y, z) on the wing surface, and $(u_{x,0}, u_{y,0}, u_{z,0})$ denote the displacements of the beam's neutral axis at the same location x along the beam axis. The resulting nodal displacements are then used to fit a second-order B-spline surface on both the upper and lower wing skins, yielding a smooth, functional representation of the displacement field over the wing.

D. Constraint Aggregation

When solving MDO problems, an important consideration is how to enforce constraints that vary over the domain on which they are defined. Classical examples of such constraints are stress, displacement, or buckling constraints that arise in structural optimization problems. Enforcing these constraints on a nodal (displacement) or element (stress) basis can quickly lead to hundreds or thousands of optimization constraints, depending on the fidelity of the model. This can significantly increase the computation time of the constraint Jacobian, and therefore the total optimization time. In practice, one is usually interested in constraining only the maximum (or minimum) value of a sizing metric such as stress or displacement. In the MDO field, this is often referred to as constraint aggregation, and the intent is to reduce the number of optimization constraints by only considering the maximum (or minimum) of a quantity of interest. However, determining the maximum value in a smooth manner suitable for solving MDO problems is non-trivial. In this work, we make use of the Kreisselmeier–Steinhauser (KS) function (implemented in CSDL) to compute the maximum or minimum of a constraint function. For a set of n constraints g_i, $(i = 1, \ldots, n)$, the KS function is given as

$$\mathrm{KS}_{\mathrm{max}}(x) = \frac{1}{\rho} \ln \left[\frac{1}{\alpha} \sum_{i}^{n} e^{\rho g_i(x)} \right], \tag{7}$$

where α is a scaling constant and $\mathrm{KS}_{\mathrm{max}}(x) \rightarrow \max_i(g_i(x))$ as $\rho \rightarrow \infty$. Several challenges may arise when using the KS function. First, the choice of ρ determines the trade-off between smoothness and accuracy. For large values of ρ, the approximation of the maximum becomes more accurate. However, near the maximum value, the gradients become large, which can lead to numerical instabilities during optimization. A reasonable choice for ρ can be determined based on the magnitude of the constraint value. Second, constraints that are not strictly active but are close to being violated can receive disproportionate influence. This is because the KS function exponentially emphasizes constraints with larger values, so constraints that are just below the maximum (but not the most critical) are still significantly amplified. This can distort the optimization process by pulling the solution towards satisfying these near-active constraints more than is necessary. Third, depending on the sensitivity of the optimized design on ρ, additional optimizations with higher values of ρ may need to be performed. For a more rigorous discussion of constraint aggregation methods for MDO problems, we refer the reader to the following references [75, 76]. Besides the structures discipline, we use the KS function to determine the maximum rotor torque and RPM across multiple one-engine inoperative (OEI) conditions.

E. Optimization Framework

In this paper, our goal is to solve a monolithic, large-scale problem with 100s of design variables and 10s of constraints. In the context of MDO, "monolithic" refers to an optimization framework in which a single optimization problem is solved that simultaneously considers all discipline models, design variables, and constraints. We denote the n-dimensional vector of design variables as $\boldsymbol{x}$, the solution to the optimization problem as $\boldsymbol{x}^*$, the objective function as $f : \mathbb{R}^n \to \mathbb{R}$, and the constraint function as $c : \mathbb{R}^n \to \mathbb{R}^m$, where m is the total number of equality and inequality constraints. An alternative to the monolithic framework is "distributed" MDO. Here, the monolithic optimization problem is divided (i.e., distributed) into N smaller suboptimization problems with objective functions $f_1, f_2, \ldots, f_N$, and constraints $c_1, c_2, \ldots, c_N$. For each suboptimization problem, the vector of design variables $\boldsymbol{x}_i$ ($i = 1, \ldots, N$), is a subset of the design variables of the monolithic problem, i.e., $\boldsymbol{x}_i \in \mathbb{R}^{l_i}$, $l_i \leq n$. The distributed architecture may be preferred if 1) numerical conditioning is an issue, 2) the monolithic problem is computationally too expensive, 3) certain sub-disciplines require specialized optimization algorithms, or 4) the MDO process is inherently distributed across multiple institutions (e.g., in industrial practice). If the problem is well-conditioned and points 2-4 are not of concern, the monolithic architecture is typically expected to converge more quickly [77].

In this work, the difficulty of using the monolithic formulation is primarily due to numerical conditioning issues, which arise from the complexity (i.e., number of considered design conditions) and heterogeneity (i.e., number of distinct disciplines). In particular, proper scaling is a challenge as design variables and constraints may span several orders of magnitude. For example, rotor speeds (RPM) can be on the order of $\sim 10^3$ while material thicknesses can be on the order of $\sim 10^{-3}$ m. The resulting scaling can lead to ill-conditioned Jacobian or Hessian matrices, which may prevent optimization algorithms from converging. In addition, a poor initial guess for the design variables can further exacerbate conditioning issues. If the initial guess leads to large constraint violations, this may result in ill-conditioned constraint Jacobian matrices, especially if constraint functions are highly nonlinear. With increasing modeling complexity and heterogeneity, finding a reasonable initial guess becomes challenging.

To address the numerical conditioning issues, we use a distributed MDO architecture to "warm-start" the monolithic problem; that is, to find a favorable initial guess and appropriate design variable scaling. The architecture is shown in Fig. 8, using the same notation as introduced previously. This warm-starting sequence can be interpreted as a single iteration of a block coordinate optimization (BCO) algorithm (see, e.g., [78]), where each subproblem is initialized with the optimized design variables of the previous sub-optimization. After solving the N-th subproblem, the monolithic problem is initialized, and the design variables are scaled according to the magnitude of the optimized design variables. For this work, we choose the subproblems based on engineering intuition and the relative size of each subproblem. In Sec. V (see Tab. 2), we present an overview of the optimization subproblems, showing which subsystems are sized in each optimization and which design conditions and constraints are applied. To solve the subproblems, we use the interior-point optimization algorithm IPOPT [79], while for the large-scale monolithic problem, we use the SNOPT algorithm [80], which is based on sequential quadratic programming. This is because interior-point algorithms are often more robust to poor variable scaling and suboptimal initial guesses. SQP-based optimizers, on the other hand, typically achieve faster convergence when the problem is well scaled and good initial guesses are available. Consequently, we use IPOPT for the subproblems and SNOPT—benefiting from the improved scaling and initialization obtained from the subproblems—for the large-scale monolithic optimization to achieve faster convergence.

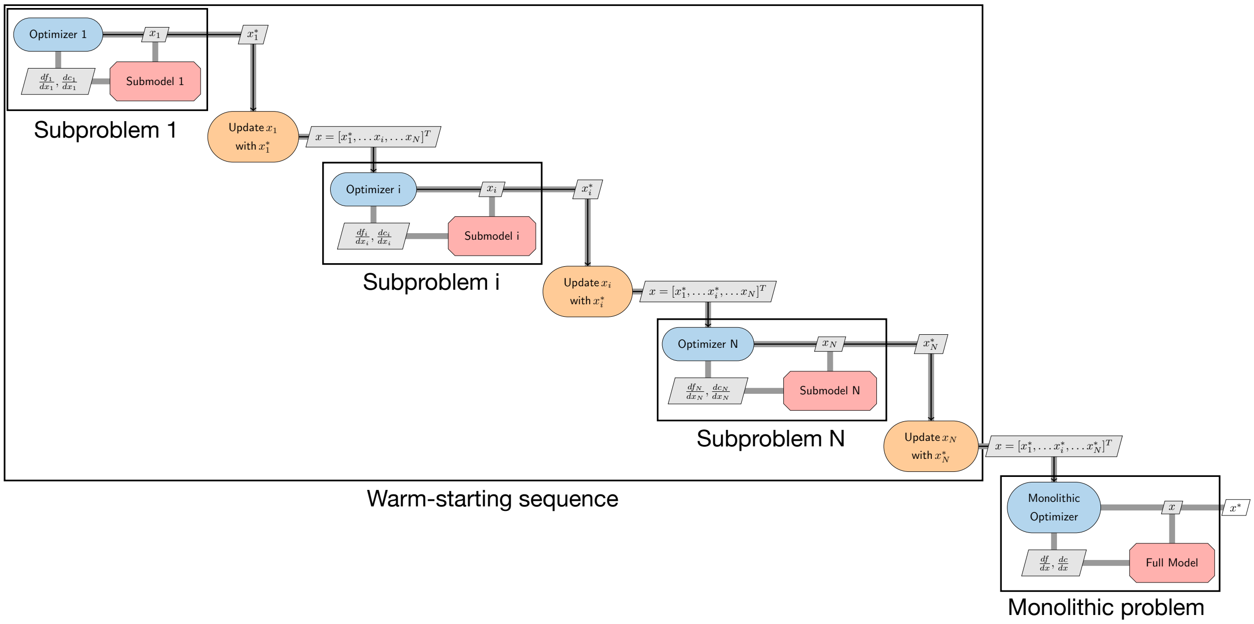

Fig. 8 XDSM of a sequence of N optimization subproblems

Lastly, we briefly address how discrete design variables can be treated within our optimization framework. Discrete design variables are challenging and can usually not be handled by gradient-based optimizers like SNOPT or IPOPT directly. In some cases (e.g., number of battery cells), discrete variables can be relaxed and treated as continuous variables during optimization and then rounded to the nearest integer once the optimizer has converged. However, for variables such as the number of rotors or spars, this is clearly not an option. While some gradient-free optimizers (e.g., genetic algorithms) can, in theory, handle discrete design variables, they scale poorly with the number of design variables and are intractable for solving large-scale problems. A more practical approach would be to optimize discrete variables in a separate (outer) optimization loop. This can be done manually, e.g., an engineer changing a small number of discrete variables like the number of rotors after each (inner) optimization run, or in automated fashion via a gradient-free algorithm. This outer-inner optimization approach in which discrete variables are optimized separately is also known as hybrid or bi-level optimization. While not used in this study, our framework supports this approach.

F. Definition of a Baseline Design

To measure the effectiveness of applying large-scale MDO to aircraft conceptual design, we need to compare the optimized design to a baseline design. At the conceptual level, an initial design is often given in terms of a set of high-level geometric (e.g., span and aspect ratio) and sizing variables (e.g., weight estimates). We denote this set of given variables $\mathcal{S}$. However, depending on the scope and type of analysis, the given design may be infeasible, or additional design variables may be needed to satisfy constraints. For example, pitch angle and elevator deflection are needed to trim an aircraft, but may not be defined in $\mathcal{S}$ as determining those variables depends on the computational models.

In this work, we propose a general definition for a baseline design that is agnostic to the computational models used for the analysis. We define the baseline design as the feasible design with the least deviation from the initial design specified by $\mathcal{S}$. The baseline design is the solution to the following optimization problem.

$$
\begin{aligned}
\min_{\mathbf{x}\in\mathbb{R}^n} \quad & f(\mathbf{x}) + \alpha\|\boldsymbol{\beta} \odot (\mathbf{x} - \mathbf{x}_0)/\mathbf{x}_0\|_2^2 \\
\text{subject to} \quad & g_i(\mathbf{x}) \leq 0, \quad i = 1, \ldots, m \\
& h_j(\mathbf{x}) = 0, \quad j = 1, \ldots, p,
\end{aligned}
\tag{8}
$$

where $\odot$ denotes the Hadamard (element-wise) product. The objective function $f(\mathbf{x})$ is augmented by a quadratic penalty term that penalizes the deviation from the initial design $\mathbf{x} - \mathbf{x}_0$, where $\mathbf{x}_0$ is the initial vector of design variables. In this penalty term, α is a scalar and $\boldsymbol{\beta}$ is a vector of binary weights that is defined as

$$
\beta_k = \begin{cases} 1 & x_k \in \mathcal{S} \\ 0 & x_k \notin \mathcal{S} \end{cases}
\tag{9}
$$

The purpose of this binary vector is to only penalize deviations from design variables that are contained in $\mathcal{S}$, i.e., design variables for which there is a baseline reference value. This deviation is measured in terms of the l^2 norm. To determine the parameter α, we perform several optimizations, varying the magnitude from 10^{-2} to 10^4. We found that a value of 10^2 works reasonably well, resulting in a design that is close to the initial design, while still being feasible. For smaller values of α, the penalization is insignificant, and for larger values, the optimizer does not converge robustly.

III. Overview of Discipline Models

In this section, we give an overview of the physics-based models used in this paper. All models are implemented using the previously described Computational System Design Language (CSDL) and therefore benefit from the automatic computation of model-output sensitivities with respect to inputs. In a recent study [81], we have shown initial verification and validation results of these models compared to established research codes and experimental data. However, the goal of this work is not to demonstrate the correctness of these models but rather their use in aircraft conceptual design using large-scale MDO.

A. Aerodynamics

We use the vortex lattice method (VLM), a low-fidelity physics-based model for predicting the lift and induced drag of lifting surfaces [82]. VLM is based on potential flow theory, and the main modeling assumptions are that the flow is incompressible, irrotational, and inviscid and that the lifting surfaces are thin with small angles of attack and sideslip.

The system of equations to be solved corresponds to the flow-tangency condition, which requires zero normal velocities across the lifting surface. In residual form, the system can be written as

$$\mathcal{R}_{\text{aero}}\left(\boldsymbol{\Gamma_b}\right) = \boldsymbol{A}\boldsymbol{\Gamma}_{\text{b}} + \boldsymbol{v} \cdot \boldsymbol{n}, \tag{10}$$

where $\boldsymbol{v}$ is the undisturbed flow velocity, $\boldsymbol{n}$ is the normal vector of the bound vortex panels. In addition, $\boldsymbol{\Gamma}_{\text{b}}$ are the bound vortex circulation strengths, and $\boldsymbol{A}$ is the aerodynamic influence coefficient (AIC) matrix. From the circulation strengths, the panel forces are calculated using the Kutta–Joukowski theorem [83] as follows

$$\boldsymbol{F} = \rho \boldsymbol{\Gamma}_{\text{b}} \boldsymbol{v}_{\text{ind}} \times \boldsymbol{s} \tag{11}$$

where ρ is the density of the air, $\boldsymbol{v}_{\text{ind}}$ is the induced velocity evaluated on the bound vortex collocation points, and $\boldsymbol{s}$ is the bound vector. The panel forces can then be summed to compute the total lift and induced drag.

B. Propulsion

In this study, we use two rotor aerodynamic models for different operating conditions. First, for hover and axial flow conditions (i.e., the rotor in-plane inflow is negligible), we use blade element momentum (BEM) theory. BEM theory combines momentum theory with two-dimensional airfoil analysis, whereby a coupled system of equations is solved to ultimately predict the sectional thrust and torque. The expressions for sectional thrust dT and sectional torque dQ derived from momentum theory are equated to their counterparts derived from blade element theory (i.e., 2-D airfoil analysis) as follows

$$dT = 4\pi\rho u_x \left(u_x - V_x\right) r dr = \frac{1}{2}\rho W^2 C_x B c dr \tag{12a}$$

$$\frac{dQ}{r} = 2\pi\rho u_x u_\theta r dr = \frac{1}{2}\rho W^2 C_\theta B c dr, \tag{12b}$$

where ρ is the air density, u_x is the total axial induced velocity at the rotor disk, u_θ is the azimuthally induced velocity at the disk, and r is the radial distance from the rotor hub. In addition, W is the resultant sectional inflow velocity, B is the number of rotor blades, c is the blade chord length, and C_x, C_θ represent coordinate transformations from the sectional inflow reference frame to the sectional thrust reference frame. These transformations are in terms of the sectional lift and drag coefficients C_l and C_d as well as the inflow angle ϕ. To solve for the sectional thrust and torque, a nonlinear equation for the inflow angle ϕ must be solved, with a residual that can be formulated as

$$\mathcal{R}_{\text{prop,BEM}}\left(\phi\right) = \frac{J}{\pi}\left(\sigma C_\theta + 4\sin\phi\cos\phi\right) + \left(\sigma C_x - 4\sin^2\phi\right), \tag{13}$$

where σ is the sectional blade solidity and J is the advance ratio. It can be shown (see e.g., [84, 85]) that a bracketed search root finding algorithm is provably convergent for most flow conditions, ensuring the robustness of the BEM computational model.

For edgewise flow cases (i.e., the rotor in-plane inflow is non-negligible), we use the Pitt–Peters [86] dynamic inflow formulation, which we solve for steady state. This model is able to capture azimuthal variations in the rotor loading with reasonable accuracy. It does so by computing the normalized axial induced inflow $\boldsymbol{\lambda}$ from three flow states, one uniform (λ_0) and two linear states (λ_s and λ_c), such that variation in the (normalized) inflow can be expressed as a function of the azimuth ψ and and the normalized radial distance $\overline{r}$ as follows:

$$\lambda(r, \psi) = \lambda_0 + \lambda_s \overline{r} \sin \psi + \lambda_c \overline{r} \sin \psi. \tag{14}$$

Pitt and Peters [86] relate the three flow states to the aerodynamic loads via the following matrix equation, given in residual form as

$$\mathcal{R}_{\text{prop, DI}} (\boldsymbol{\lambda}) = \boldsymbol{M}_{\text{prop}} \dot{\boldsymbol{\lambda}} + \boldsymbol{L}^{-1} \boldsymbol{\lambda} - \boldsymbol{c}, \tag{15}$$

where the aerodynamic loads $\boldsymbol{c}$ are in terms of the thrust coefficient C_T and the moment coefficients C_L and C_M. These coefficients are determined from blade element theory by integrating and normalizing the right-hand side of Eq. (12a). The derivative matrix $\boldsymbol{L}$ and mass matrix $\boldsymbol{M}_{\text{prop}}$ are given in various sources(see e.g., [86, 87]). In this work, we neglect transient effects and solve Eq. (15) for steady state. It is important to note that the flow state vector $\boldsymbol{\lambda}$ depends on the aerodynamic loads $\boldsymbol{c}$, making Eq. (15) a nonlinear residual that is solved via a Newton algorithm.

C. Airfoil Modeling

Many low-to mid-fidelity physics-based aerodynamic models, such as the VLM or BEM methods, discretize lifting surfaces or rotors spanwise and embed an airfoil model to augment the analysis. Typical quantities of interest are scalar-valued quantities such as the lift and drag coefficients (C_l, C_d) as well as vector-valued quantities such as the pressure profile or boundary layer parameters like momentum or displacement thickness, which vary along the boundary of the airfoil. Any quantity of interest can be represented as a function of the airflow, characterized by the angle of attack α, Reynolds number Re, Mach number Ma, and the airfoil shape. For this study, we train surrogate models using artificial neural networks (ANN) based on aerodynamic training data obtained from XFOIL [88], a widely used subsonic 2-D panel code with boundary layer models for laminar and turbulent regimes. We consider a wide range of Reynolds numbers (10^5 to 8×10^6), Mach numbers (0 to 0.5), and angles of attack (pre-stall). For certain analyses, like rotor aerodynamics, it is important that the airfoil model is well-defined beyond the stall region. We use the Viterna method [89] to extrapolate the airfoil polar to angles of attack of $\pm 90°$.

A well-trained airfoil model can significantly enhance the predictive capabilities of low-fidelity aerodynamic models.

In the case of rotor-aerodynamic analysis, there are significant variations in all three flow states as certain sections of the blade may be stalled, and relative inflow speeds increase toward the rotor tip. An airfoil model should therefore be able to capture these effects. Moreover, an airfoil model can be combined with 3D aerodynamic models like VLM to predict vector-valued quantities like the pressure profile or boundary layer parameters at discrete sections along the spanwise direction. To achieve this, a spanwise lift coefficient is determined from the VLM solution and treated as the true solution. The airfoil model is then queried to find the corresponding angle of attack via a bracketed search (bisection) algorithm. We denote this angle of attack α^* and emphasize that it is different than the angle of attack of the airfoil with respect to the free-stream flow direction , due to the induced velocity (i.e., downwash) generated by the finite wing. Then, the airfoil model is evaluated at α^* (and the corresponding Reynolds and Mach number) to compute the desired quantity of interest, denoted $\boldsymbol{q}$. Mathematically, this process is expressed as follows:

$$\mathcal{R}_{\text{airfoil}}(\alpha) = C_{l,\text{VLM}} - C_{l,\text{airfoil}}(\alpha) \rightarrow \alpha^* \tag{16a}$$

$$\boldsymbol{q} = f(\alpha^*, \text{Re}, \text{Ma}). \tag{16b}$$

In this work, we use this approach to predict the pressure profile over the wing of the aircraft to determine the aerodynamic loads acting on the structural mesh (integrated pressures). The VLM solution itself does not suffice for this purpose since it is defined on the camber surface mesh rather than the upper and lower wing surfaces.

In summary, the spanwise lift coefficients from the VLM solution are used to calibrate the local angles of attack for a finite set of airfoils along the wing span, which are then used by an XFOIL-based machine learning model to compute a 2D pressure distribution for each airfoil. These 2D pressure distributions are then interpolated along the wing span to estimate a 3D pressure field over the wing surface, which is used to define the wing loads for structural (wing) weight estimation.

Lastly, in Fig. 9, we verify the two airfoil models used in this study. For the wing, we use a NASA GA(W)-2 airfoil and for the rotors and propeller, we use use a NACA 0012 airfoil. For the C_p model we used a total of 1908 samples (each of size 240) and achieved a root mean squared error (RMSE) of 0.039 for the validation set (573 samples). For the C_l and C_d models, we used 5839 (scalar) samples each, and the RMSE was 0.005 (C_l) and 0.001 (C_d) for the validation set (1752 samples each).

D. Structures and Weights

Structural weight estimation techniques for conventional aircraft often rely on statistical methods or simple, energy-based formulas. Unconventional aircraft, including many UAM concepts, cannot use these methods because the configuration of the aircraft is unique and is not well represented by existing data. This limitation motivates the use of physics-based structural weight estimation for sizing UAM-like aircraft. In this work, we adopt a linear Euler–Bernoulli

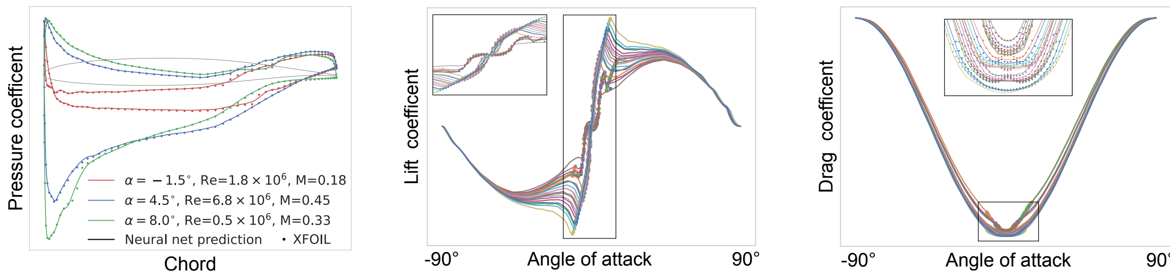

(a) Pressure coefficient for NASA GA(W)-2 airfoil

(b) Extrapolated lift polar of NACA 0012 airfoil

(c) Extrapolated drag polar of NACA 0012 airfoil

Fig. 9 Verification of airfoil surrogate models

(EB) beam model developed by Orndorff et al. [56], which approximates long and slender structural components as one-dimensional beams. A key assumption of the EB model is the neglect of transverse shear deformation, making it most suitable for slender members (e.g., wing boxes) dominated by bending. For aircraft conceptual design, beam models strike an effective balance between computational efficiency and fidelity. While they neglect localized effects such as stress concentrations, joint flexibility, and detailed load paths, they capture the global bending and deflection behavior of major load-carrying members reasonably well. Additionally, their low computational cost and numerical robustness make them particularly attractive for use in large-scale MDO problems.

The structural system is represented by a global stiffness matrix $\boldsymbol{K}$. When applying a load vector $\boldsymbol{f}_{\text{nodal}}$, the nodal displacements $\boldsymbol{u}_{\text{nodal}}$ are found by solving a single linear system, which written in residual form, is

$$\mathcal{R}_{\text{struct}}\left(\boldsymbol{u}_{\text{nodal}}\right) = \boldsymbol{K}\boldsymbol{u}_{\text{nodal}} - \boldsymbol{f}_{\text{nodal}}. \tag{17}$$

The stiffness matrix is constructed using 12×12 frame stiffness elements [74]. These elemental stiffness matrices use simple tube and box-beam representations when computing cross-sectional properties. For example, a wing can be reasonably represented by a box-beam and a fuselage by a tube [90] [91]. By optimizing the thicknesses of the cross-section in question, we can find the minimum-mass structure given certain constraints. The most basic constraint is the maximum allowable stress or displacement. However, many slender structures like wings will instead be sized by buckling constraints. To capture this, we calculate the critical buckling stress for curved plates as a function of the skin thickness t, the plate width b, and the radius of curvature r' based on Roark's work [92] as follows.

$$\sigma' = \frac{1}{6}\frac{E}{1-\nu^2}\left(\sqrt{12(1-\nu^2)\left(\frac{t}{r'}\right)^2 + \left(\frac{\pi t}{b}\right)^4} + \left(\frac{\pi t}{b}\right)^2\right) \tag{18}$$

The radius of curvature r' is determined from the central geometry for each panel using the SIFR methodology. For stress-constrained structures, we perform a stress-recovery based on the nodal displacements and a selection of stress-evaluation points on the cross section. For box beams, the Von-Mises stress is evaluated at five points that are expected to capture the maximum axial, bending, and shear stresses reasonably well under typical loading conditions [90].

For this study, the material of choice is aluminum alloy. In theory, the beam solution can be combined with composite laminate theory (CLT) for the side panels, to model composite materials. However, this approach would add computational complexity and would only be appropriate for simple cross sections. Due to the limitations of the box-beam model, which assumes constant cross-sectional properties (i.e., we cannot model stiffeners), we expect to over-predict the mass of the wing box and do not apply a safety factor for buckling constraints. To capture variations in the cross-sectional properties, higher-order beam models such as the variational asymptotic method (e.g., [93]) or shell models are necessary.

Lastly, we note that the beam model is used only to size the wing box. For the other structural components we consider—fuselage, empennage, booms—we use weight regression models developed specifically for the lift-plus-cruise concept [41], which is the configuration we consider in this study. The regressions are based on data obtained from parametric finite element models (NASTRAN) of about 100 different configurations of the lift-plus-cruise vehicle. These configurations were generated by sampling (Latin hypercube) the following parameters: wing area, wing aspect ratio, tail area, tail aspect ratio, fuselage length, battery weight, and cruise speed. For each configuration, a total of eight load cases were considered, including transition loads, one-engine-inoperative loads, as well as forward and downward crash loads.

E. Aeroacoustics

The dominant noise sources that are typically considered at the conceptual level are tonal and broadband noise. For tonal noise, we use a frequency domain model developed by Lowson and Ollerhead [94] (LO) to predict the loading noise component of the tonal noise. The model accounts for variations in the aerodynamic loading along the azimuth, which makes it suitable for edgewise flow conditions. It does so by representing the azimuthally varying loads (at a given radial location) using a Fourier series expansion as follows:

$$\boldsymbol{f}_{\text{aero}}(\psi) = a_{0T} + \sum_{\lambda=1}^{\infty} a_\lambda \cos(\lambda\psi) + b_\lambda \sin(\lambda\psi), \tag{19}$$

where $\boldsymbol{f}_{\text{aero}}$ represents either thrust or drag. The Fourier coefficients a_λ and b_λ can be determined by solving a linear system, which can be written in residual form as

$$\mathcal{R}_{\text{tonal}}\left(\boldsymbol{a}_f\right) = \boldsymbol{H}\boldsymbol{a}_f - \boldsymbol{f}_{\text{aero}}, \tag{20}$$

where $\boldsymbol{H}$ is the matrix constructed from cosine and sine terms evaluated at the given azimuthal coordinates, $\boldsymbol{f}_{\text{aero}}$ is the vector of azimuthally varying loads, and $\boldsymbol{a}_f$ is the unknown vector of Fourier coefficients. These coefficients are used in combination with information regarding the blade geometry, rotor speed, and observer location to determine the total sound pressure level as

$$\text{SPL}\left(\boldsymbol{a}_f\right) = 10\log_{10}\left(\frac{|g(\boldsymbol{a}_f)|^2}{2P_{ref}^2}\right), \tag{21}$$

where the form of g is adopted from Lowson and Ollerhead [94] and $P_{ref} = 2 \times 10^{-5}$. We make several modifications to the LO model to address some of its shortcomings. First, it only predicts loading noise, which is dominated by blade thickness noise when the observer location is in the rotor plane. Therefore, we add a thickness noise model proposed by Barry and Magliozzi [24, 95], which is valid for hover and axial forward flight. Second, in hover, the LO model reduces to Gutin's [96] formulation, which is known to significantly under-predict the loading noise along the rotor axis (see, e.g., [24]). To address this issue, we use the Sears function [97] to account for azimuthal variations in the aerodynamic loading due to unsteady aerodynamic effects like gusts that are otherwise not captured by steady aerodynamic models like blade element momentum (BEM) theory. The use of the Sears function to predict loading noise in hover was first proposed by Kvurt and Stalnov [98]. Third, to account for the motion of the rotor hub, a Doppler correction is applied to the hub-obsever distance using the Mach number in the direction of the observer.

For modeling broadband noise, we use a recently developed spectrum model by Gill and Lee (GL) [25] to predict the broadband noise spectrum and the overall sound pressure level (OASPL). The GL model is a data-driven empirical broadband noise spectrum model that was developed using an evolutionary machine learning algorithm called Gene Expression Programming (GEP). Experimental data from modern rotors, such as drone rotors [99, 100] and UAM rotors [101], was used as training data in the GEP algorithm. A detailed description of the machine learning algorithm can be found in these references [25, 102, 103]. The pre-determined functional form of this model is given as

$$\text{SPL}_{1/3} = \frac{f_0\left[S_t - (f_1\log_{10}C_T + f_2\log_{10}\sigma)\right]^{0.6}}{[f_3\Delta^{f_4} + f_5]^{f_6} + [f_7\Delta]^{f_8}}, \tag{22}$$

where S_t is Strouhal number based on the solidity-weighted chord length, C_T is thrust coefficient, and σ is rotor solidity. The assumed form of the GEP spectrum model is based on a universal wall pressure spectrum model [104] since this wall pressure spectrum determines the primary shape of trailing-edge noise [105], which is a major rotor broadband noise source [106]. In Eq. (22), the functions f_1 through f_8 are obtained by the GEP algorithm, while the function f_0 is in terms of the rotor tip speed and controls the amplitude of the spectrum. The complete set of functions is given by Gill and Lee [25]. Although this model is derived from a series of experiments on rotors in hover, preliminary validations show reasonable predictive performance even for axial and edgewise forward flight conditions [81].

F. Motor Analysis

The motor discipline plays an important role in weight estimation and power consumption for electric aircraft. At the system level, electric motors are commonly represented with simple models, assuming a constant efficiency [107] and a specific torque [108] or power [109]. These methods do not capture the dependence of motor performance on the geometry and are not viable for off-design conditions (like one-motor out) and sizing cases, where power demand significantly rises and efficiency is no longer constant. We require a motor model that is flexible enough to capture a broad range of operating conditions and runs quickly. To this end, we use the motor model developed by Cheng et al. [110], which is applicable for the design and analysis of in-runner permanent magnet synchronous motors (PMSMs) with embedded magnets. The method includes both sizing and analysis methods.

The motor sizing model determines the internal motor geometry and follows the approach developed in [111]. The inputs to the model are motor length L and outer diameter D, commonly treated as design variables, along with electric loading $\bar{A}$ and magnetic loading $\bar{B}$. These are used to compute high-level geometry parameters, such as shaft diameter and rotor diameter, along with the detailed design of the internal motor structure, such as the stator tooth dimensions and air-gap thickness. A detailed summary of these parameters and respective formulas is given in [110]. We compute the mass using a constant specific torque and the same set of inputs:

$$m = \frac{\pi \bar{A} \bar{B} D^2 L}{2 Q_{sp}}, \tag{23}$$

where Q_{sp} is the specific torque.

The motor analysis model uses equivalent circuit models (ECM) and motor control methods to estimate motor performance based on rotor torque and RPM. The equivalent circuit models are derived from the motor structure and determine operating parameters such as magnet flux strength and motor inductance. With these parameters, the motor performance model determines the operating electromagnetic (EM) torque T_{em} that meets the input rotor torque. The EM torque is found implicitly with the motor efficiency η:

$$\mathcal{R}_\eta \left(T_{em}\right) = \eta T_{em} - \tau_{load}, \tag{24}$$

where the efficiency η is a function of the EM torque. The method uses the maximum-torque-per-ampere (MTPA) control strategy [112] to compute the operating current. The MTPA control strategy is based on finding the operating current that satisfies the conditions

$$\begin{cases} \dfrac{\partial \frac{T_{em}}{I_{lim}}}{\partial I_d} = 0, \\ \dfrac{\partial \frac{T_{em}}{I_{lim}}}{\partial I_q} = 0, \end{cases} \tag{25}$$

where the subscripts d and q (direct-quadrature) denote the components in the d-q axis system . Combining these conditions with the equivalent circuit motor model, the q-axis current I_q that satisfies MTPA is found by implicitly solving a quartic equation:

$$\mathcal{R}_{\text{MTPA}}\left(I_q^*\right) = I_q^{*4} + T_{em}^* I_q^* - T_{em}^{*2}, \tag{26}$$

where the superscript $*$ denotes per-unit values. Further details of this derivation are provided in [110].

The motor model includes a flux-weakening control strategy [113] for motor operation at high speeds and near the voltage limit. A novel control smoothing method was developed to maintain differentiability between the two control methods. In this work, however, we do not consider flux-weakening since the rotor speed is unlikely to enter the region of the torque-speed space where flux-weakening is critical.

G. Battery

In this study, we employ a simplified approach to battery sizing and analysis. The optimizer directly controls the battery mass, designated as m_{bat}. For a given a battery mass m_{bat} and a battery energy density ρ_{bat} (Wh/kg), the total energy capacity of the battery (E_{total}) is calculated as

$$E_{\text{total}} = (\rho_{\text{bat}} \cdot 3600)\left(\frac{m_{\text{bat}}}{1000}\right) \tag{27}$$

We assume a future battery technology with a pack-level energy density of 400 Wh/kg. Denoting the power profile as $P(t)$, time as t, and the total mission time as T, the end-of-mission state-of-charge is determined by

$$SoC = E_{\text{total}} - \frac{\int_0^T P(t)dt}{E_{\text{total}}}. \tag{28}$$

The power for each mission segment is calculated and then multiplied by its corresponding duration to determine the energy expenditure.

H. Flight Dynamics and Stability Analysis

In this work, we use a set of rigid-body equations of motion with six degrees of freedom, expressed in a body-fixed reference frame based on the Euler angles. This model assumes that the Earth is flat, that its rotation is negligible, and that the atmosphere is at rest. Furthermore, the aircraft's moment of inertia is assumed to be constant, and rotations of subsystems (e.g., rotors) are neglected. We present these equations in the Appendix (see Eq. (34)) and refer the reader to the following references for further details [114, 115]. In matrix form, the system of equations can be written as

$$\mathcal{R}_{\text{eom}}(\boldsymbol{a}) = \boldsymbol{M}_{\text{eom}}\boldsymbol{a} - \boldsymbol{f}, \tag{29}$$

where $\boldsymbol{M}_{\text{eom}}$ is a 6×6 mass properties matrix, $\boldsymbol{f}$ is the vector of the total forces and moments acting on the aircraft, and $\boldsymbol{a}$ is the acceleration vector containing the linear accelerations $\dot{\boldsymbol{v}}$ and the angular accelerations $\dot{\boldsymbol{\omega}}$. For steady design conditions, the residual in Eq. (29) is driven to zero such that the net acceleration is zero to achieve trim. For quasi-steady conditions, a subset of the acceleration vector is constrained to follow a discretized trajectory while the remainder is driven to zero. Lastly, in addition to trim, we consider static longitudinal stability by computing the static margin normalized by the mean aerodynamic chord (MAC). To determine the neutral point (NP), we formulate the pitching moment sensitivity with respect to the angle of attack as a residual where the state variable is the x-location along the fuselage, such that

$$\mathcal{R}_{NP}(x) = \frac{\partial M_y(x)}{\partial \alpha}, \tag{30}$$

where M_y is the pitching moment, α is the angle of attack, and x is the distance from the nose of the aircraft. The residual is driven to zero by a bracketed search algorithm (i.e., the bisection method) where the nose and tail of the fuselage define the bracket.

I. Summary of Discipline Models

To conclude Sec. III, we summarize all computational models used in this work in Fig. 10, emphasizing that most models (except the motor performance model, the weight regressions, and the battery model) are directly connected to and dependent on the central geometry (see Sec. II.B). The central geometry model is responsible for updating solver meshes (e.g., VLM), force locations (e.g., rotor thrust), and center of gravity locations (e.g., motor weight) to reflect changes in planform design variables like wing area during optimization and to enforce kinematic constraints (e.g., boom-to-wing connections). In addition, the central geometry model is critical to the SIFR methodology (see Sec. II.C.2), to define field quantities over the OML, which is shown notionally for the structures and aerodynamics disciplines, where field quantities (pressure and displacements) are represented in functional form. Lastly, Table 1 provides a summary of all residual equations (linear and nonlinear) that arise in our computational models with a brief description of the state variables and the numerical solvers.

IV. Design Problem Based on NASA Lift-Plus-Cruise Concept

For this work, we consider a lift-plus-cruise Urban Air Mobility (UAM) reference vehicle proposed by NASA, which is described in detail by Silva et al. [116]. The vehicle concept was developed for manned and unmanned operations and features a distributed electric propulsion architecture. The lift-plus-cruise concept has eight lift rotors that are only operated during takeoff and transition periods. During the climb, cruise, and descent segments, the vehicle operates as a fixed-wing aircraft with a pusher propeller mounted at the rear of the vehicle. Some of the envisioned advantages of the lift-plus-cruise configuration are a reduced noise footprint due to slower rotor tip speeds, multicopter-like redundancy,

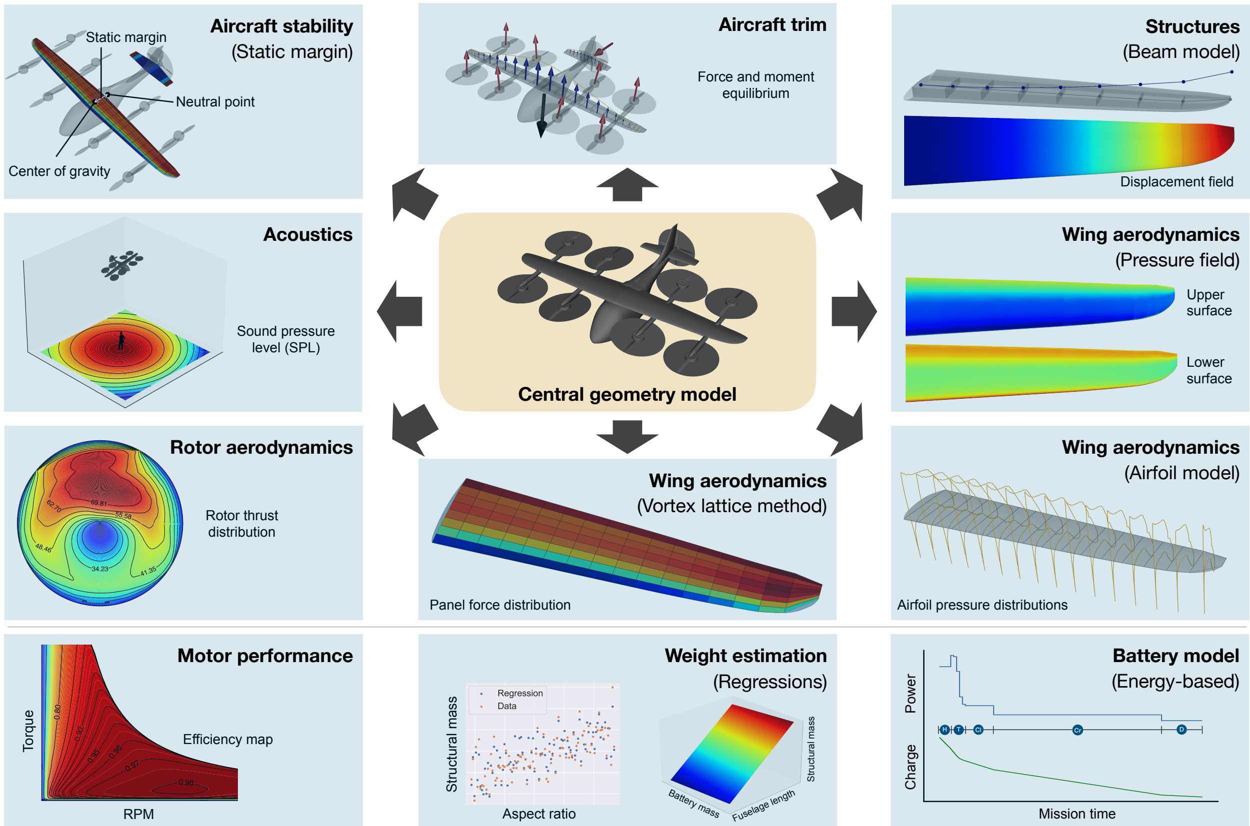

Fig. 10 We demonstrate the solution of a large-scale MDO problem that involves all the major disciplines relevant in aircraft conceptual design (aerodynamics, structures, aeroacoustics, propulsion, motor performance, aircraft trim and stability, weight estimation, and battery analysis) using a geometry-centric approach

.

Table 1 Summary of residual equations across all disciplines.

Discipline	Residual	Reference	Type	State variable	Numerical solver
Geometry	$\mathcal{R}_{\text{geo}}(x)$	Eq. (3)	Nonlinear	B-spline control points	Newton
Wing aerodynamics	$\mathcal{R}_{\text{aero}}(\Gamma_b)$	Eq. (10)	Linear	Bound vortex circulation strength	Direct
Rotor aerodynamics	$\mathcal{R}_{\text{prop,BEM}}(\phi)$	Eq. (13)	Nonlinear	Sectional inflow angle	Bisection
	$\mathcal{R}_{\text{prop,DI}}(\lambda)$	Eq. (15)	Nonlinear	Constant and linear inflow	Newton
Airfoil	$\mathcal{R}_{\text{airfoil}}(\alpha)$	Eq. (16a)	Nonlinear	Angle of attack	Bisection
Structures	$\mathcal{R}_{\text{struct}}(u_{\text{nodal}})$	Eq. (17)	Linear	Nodal displacements	Direct
Aeroacoustics	$\mathcal{R}_{\text{tonal}}(a_f)$	Eq. (20)	Linear	Fourier coefficients	Direct
Motor	$\mathcal{R}_{\eta}(T_{em})$	Eq. (24)	Nonlinear	Electromagnetic torque	Newton
	$\mathcal{R}_{\text{MTPA}}(I_q^*)$	Eq. (26)	Nonlinear	q-axis current	Bisection
Aircraft trim	$\mathcal{R}_{\text{eom}}(a)$	Eq. (29)	Linear	Accelerations	Direct
Aircraft stability	$\mathcal{R}_{\text{NP}}(x)$	Eq. (30)	Nonlinear	Location for neutral-point computation	Bisection

and smaller batteries due to high aerodynamic efficiency when operating as a fixed-wing aircraft. Both fully-electric and hybrid-electric powertrain architectures were explored, and in this paper, we consider the fully-electric architecture.

The proposed sizing mission profile for the lift-plus-cruise vehicle is described in detail by Silva et al. [116]. The nominal mission begins with a taxi followed by a vertical climb to 250 ft above the ground and a 30-second hover period before transitioning to forward flight at a constant altitude. After the outbound transition, the vehicle climbs at a rate of no less than 900 ft/min to an altitude of 3280 ft. The aircraft then cruises at a Mach number of 0.17 for a distance of 43 miles, after which the aircraft descends to an altitude of 250 ft. Next is an inbound transition to hovering flight before descending vertically. The same mission is then repeated a second time. For safety, a reserve mission equal to a single cruise segment is included to ensure the aircraft can safely land at an alternate location in case of an emergency. The taxi, vertical ascent, inbound transition, and vertical descent segments are not modeled in this work. This is, in part, because the physics-based models chosen for this study lack the fidelity to appropriately model some of these conditions. For example, the rotor-aerodynamic model (dynamic inflow) is not well suited for simulating the inbound transition or vertical descent, as these conditions involve negative inflow, wherein the aircraft encounters its own wake. To compensate for the omission of these segments in the total mission power calculation, the hover segment duration is increased from 30 to 60 seconds, and the power of the outbound transition is doubled to account for the excluded inbound transition.

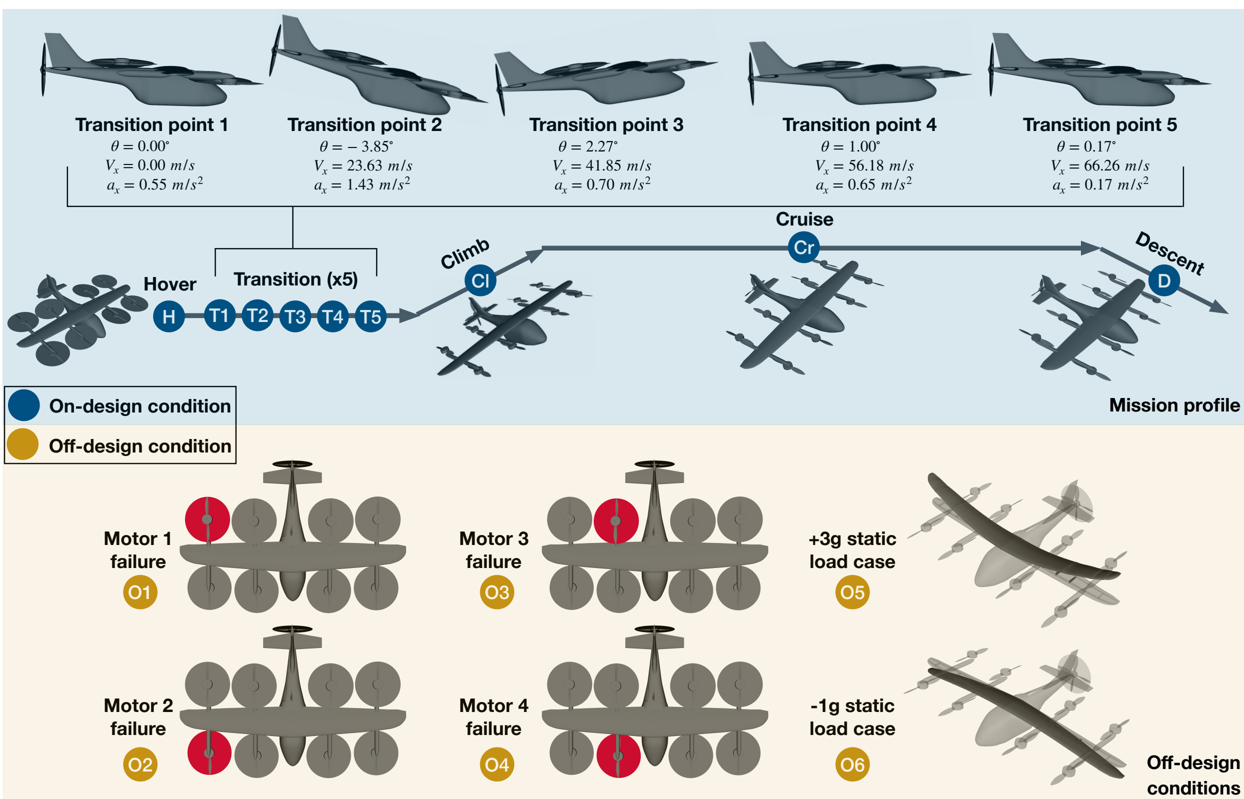

Fig. 11 Our large-scale design problem involves a comprehensive set of design conditions, including a nominal mission (hover, quasi-steady transition, climb, cruise, descent) and off-design sizing conditions (motor failure and static structural sizing conditions). In total, we consider 15 design conditions.

For the constant-altitude outbound transition, we use results published by van Schie et al. [117] based on Tagg et al. [19], who used the vortex particle method to compute a minimum-energy trajectory of the lift-plus-cruise vehicle. We discretize this profile with five quasi-steady points at which we prescribe the vehicle's speed and pitch angle and constrain the accelerations to match those of the minimum energy trajectory. In addition to the nominal mission segments, we consider two static structural sizing cases (+3g/-1g) that size the wing as well as four one-engine inoperative (OEI) cases (one for each lift rotor on either side) in hover that will size the lift motors. Figure 11 summarizes the design conditions that we model in this work, divided into on-design conditions and off-design conditions. On-design conditions refer to operational states that are expected during a nominal mission (e.g., climb, cruise) while off-design conditions constitute unforeseen scenarios such as one-engine-inoperative (OEI) conditions or extreme structural load cases for which the aircraft needs to be sized. In total, we consider 15 design conditions.

Lastly, we describe our approach for computing the gross weight of the lift-plus-cruise vehicle, which is the objective of our large-scale MDO study, discussed in the next section. At a high level, the gross weight computation is as follows.

$$W_0 = W_{\text{structures}} + W_{\text{battery}} + W_{\text{powertrain}} + \overbrace{W_{\text{payload}}}^{540\,\text{lb}} + \overbrace{W_{\text{systems}}}^{270\,\text{lb}} + \overbrace{W_{\text{other}}}^{880\,\text{lb}} \tag{31}$$

The terms W_{payload}, W_{systems} are held constant based on results by Silva et al. [116], who performed the initial sizing of the lift-plus-cruise reference vehicle using the NASA-developed tools NDARC [7] and CAMRAD II such that the vehicle can complete the previously described mission profile. Because the NASA reference paper did not provide details on all weight components, W_{other} (also constant) was chosen so that the initial gross weight computed by our computational model matches closely with the NASA reference.

The total structural weight is composed of four components, such that

$$W_{\text{structures}} = W_{\text{wing}} + W_{\text{fuselage}} + W_{\text{empennage}} + W_{\text{booms}}, \tag{32}$$

where W_{wing} is estimated using the beam model, and W_{fuselage}, $W_{\text{empennage}}$, and W_{booms} are estimated using the regression models described at the end of Sec. III.D. Next, the battery weight W_{battery} is a design variable directly controlled by the optimizer. This is possible due to the simplicity of our energy-based battery model. Lastly, the powertrain weight has two components.

$$W_{\text{powertrain}} = W_{\text{motor}} + W_{\text{power electronics}} \tag{33}$$

The motor weight is computed as a function of the motor width and length (see Eq. 23) and the weight of the power electronics (e.g., inverters and filters) is held constant at about 90 lb. This number was obtained from results by van Schie et al. [117], based on work by Cheng et al. [118], who performed a powertrain topology optimization of the lift-plus-cruise vehicle.

The computation of the vehicle gross weight is tightly coupled with the mission analysis. At each optimization iteration, the gross weight is computed as described above and provided to the mission analysis (i.e., on-design conditions) and off-design conditions. For each design condition, the various discipline models compute operational constraints (see Sec. V.B) such as aircraft trim, structural failure modes, motor torque margins, noise emissions, battery state of charge, and others. These constraints are dependent on the gross weight as well (fixed) mission parameters such as time spent in hover, climb rate, or cruise range. Each constraint is fed back to the optimizer, which iteratively drives the design toward feasibility.

V. Results

As discussed in Sec. II.E, we use a warm-starting strategy to determine favorable design variable scaling and a reasonable initial guess for the full-scale monolithic problem. In Table 2, we provide an overview of the different subproblems, showing which subsystems are sized in each subproblem, based on the primary sizing conditions and relevant constraints. In addition, Table 3 shows the coupling variables between the subproblems. Given that our MDO approach relies on adjoint-based sensitivity analysis, we compare the analytic gradients against a (first order) finite difference approximation for decreasing step sizes. The results are shown in Fig. 12 for the subproblems. The remainder of this section is organized as four subsections. In Sec. V.A, we share results from the aeroelastic optimization (subproblem 3). We highlight the effect of constraint aggregation and the effect of resolving the aeroelastic coupling on the optimized wing structure. In Sec. V.B, we share the results of solving the full-scale MDO problem, where we investigate the effect of a static margin constraint on the optimized design. Next, in Sec. V.C, we present a set of parameter sweeps, where we vary the battery energy density and final battery state of charge (SoC). Lastly, we provide statistics of the computational model and the optimization problems in Sec. V.D.

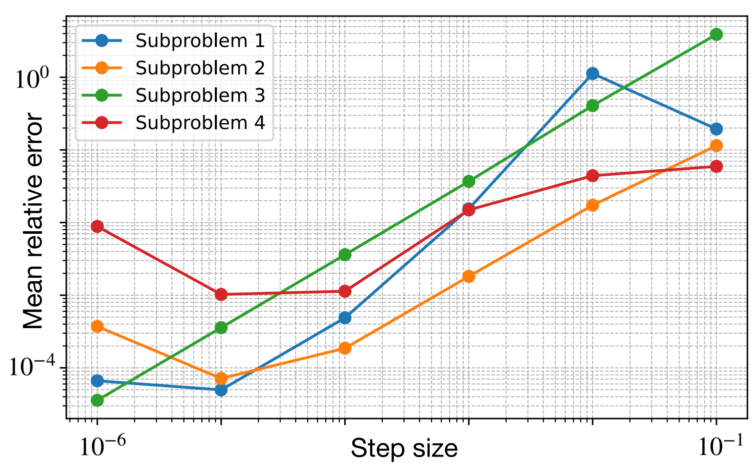

Fig. 12 Verification of analytical adjoints via finite difference comparison

Table 2 Summary of optimization subproblems

Subproblem	Subsystems	Sizing conditions	Design variables	Constraints
1	• Rotors • Battery • Pusher motor	• Hover • Transition • Climb • Cruise • Descent	• Rotor speeds (pusher, lift) • Aircraft pitch • Elevator deflection • Battery mass • Pusher motor length	• Aircraft trim • Total noise (hover) • Final state-of-charge • Motor torque safety margin
2	• Lift motors	• OEI	• Rotor speeds (lift) • Lift motor lengths	• Aircraft trim • Motor torque safety margins
3	• Wing box	• Static load cases • +3g • -1g	• Skin thickness • Spar thickness • Aircraft pitch	• Simplified trim • Structural failure
4	• Planform	• Cruise	• Reference area (wing/tail) • Aspect ratio (wing/tail) • Fuselage length • Rotor speed (pusher) • Aircraft pitch • Elevator deflection	• Aircraft trim • Static margin

Table 3 Coupling between optimization subproblems

From ↓ / To →	Subproblem 1	Subproblem 2	Subproblem 3	Subproblem 4
Subproblem 1	–	• Battery mass • Pusher motor length	• Battery mass • Pusher motor length	• Battery mass • Pusher motor length • Aircraft pitch • Elevator deflection • Rotor speed (pusher)
Subproblem 2	• Lift motor lengths	–	• Lift motor lengths	• Lift motor lengths
Subproblem 3	• Skin thickness • Spar thickness	• Skin thickness • Spar thickness	–	• Skin thickness • Spar thickness
Subproblem 4	• Reference area (wing/tail) • Aspect ratio (wing/tail) • Fuselage length • Aircraft pitch • Elevator deflection • Rotor speed (pusher)	• Reference area (wing/tail) • Aspect ratio (wing/tail) • Fuselage length	• Reference area (wing/tail) • Aspect ratio (wing/tail) • Fuselage length	–

A. Structural Sizing

We size the initial wing structure based on two loading conditions: a +3g and a -1g static load. For aircraft trim, we only consider force equilibrium in the z-direction. For the load and displacement transfer, we consider two cases: a one-way coupled case in which the aerodynamic loads are transferred onto the beam structure, and a two-way coupled case where we also consider the wing displacement in the aerodynamic solver. We use the SIFR methodology (see Sec. II.C.2) for the load and displacement transfer and use a Jacobi iteration to resolve the coupling. The design variables for this problem are the thicknesses of the wing box, and we enforce panel buckling, stress, and displacement constraints. The material is assumed to be aluminum. Due to the curved wing-tip geometry of the lift-plus-cruise concept, we enforce the plate buckling constraint on all the skin panels except the last panel at the wing tip , while the stress and displacement constraints are applied to all beam elements and nodes (nine total nodes for one-half of the wing). The optimization problem is shown in Table 4 with and without constraint aggregation via the KS function. For the stress constraint, we note that we have five stress recovery points at each beam cross-section. We see that aggregating the constraints reduces the number of constraints by about one order of magnitude.

Table 4 Structural optimization problem

	Variable/function	**Quantity**
minimize	wing structural mass	
w.r.t.	front spar thickness	8
	rear spar thickness	8
	top skin thickness	8
	bottom skin thickness	8
	aircraft pitch angle	2
	# design variables	34
subject to (aggr./non-aggr.)	buckling constraints	2 / 14
	stress constraints	2 / 80
	z-displacement constraints	2 / 18
	z-force equilibrium	2
	# constraints	8 / 114

We show the results of the structural optimization in Table 5, in terms of the optimized wing mass, high-level optimization parameters like optimization time and number of optimization iterations, as well as which constraints are active. In addition, we show the optimized top and bottom skin thicknesses in Fig. 13 from the wing root (left) to the wing tip (right). We note that the outermost top and bottom skin panels are sized to minimum gauge (0.3 mm) since we do not enforce the panel buckling constraint there due to the curved geometry of the wing near the tip. The most significant result is that the optimized wing structural mass is insensitive to the coupling scheme as well as whether constraint-aggregation is used or not. The largest deviation in mass is about 0.1% between the two-way coupled, non-aggregated test case and the one-way coupled, aggregated test case. Based on the significant increase in optimization time (about two orders of magnitude) when considering the two-way coupled load-and-displacement transfer, we conclude that for the considered load cases, the improvement in accuracy does not justify the increased run time. Therefore, for the full-scale optimization, we only consider the one-way coupled case.

For the one-way coupled case, using the KS function to aggregate the constraints significantly reduces the optimization time by about 60%. This is primarily due to the decreased derivative function evaluation time (specifically the constraint Jacobian), which is about one order of magnitude lower when using constraint aggregation. However, we also see that when the constraints are aggregated, the number of optimization iterations increases by more than two times, indicating slower convergence, most likely due to an increase in numerical noise. Regarding the constraints, the displacement constraint remains inactive along the entire beam. The stress distribution, shown in Fig. 14, indicates that the stress constraint is active only in the innermost shear (spar) panel. For the top and bottom skin panels, the stress constraint is inactive, suggesting that buckling (always active) is the primary sizing constraint. Therefore, we will only consider the buckling constraint in the full-scale optimization problem, which reduces the number of structural constraints significantly. This allows us to avoid the previously described challenges of using the KS function in large-scale MDO problems by not aggregating the buckling constraints without incurring a large penalty in derivative evaluation time.

Table 5 Results of wing structural optimization of initial design

Stress (< 350 MPa)	*Aggr.*	*Non-Aggr.*	**Wing mass (kg)**	*Aggr.*	*Non-Aggr.*
One-way coupled	Active (+3g) only at innermost shear panel	Active (+3g) only at innermost shear panel	*One-way coupled*	354.9	354.3
Two-way coupled			*Two-way coupled*	354.8	354.2
Displacement (< 0.5 m)	*Aggr.*	*Non-Aggr.*	**Function time (s)**	*Aggr.*	*Non-Aggr.*
One-way coupled	Inactive (max 0.24 m)	Inactive (max 0.21 m)	*One-way coupled*	0.06	0.05
Two-way coupled			*Two-way coupled*	0.26	0.25
Buckling	*Aggr.*	*Non-Aggr.*	**Derivative time (s)**	*Aggr.*	*Non-Aggr.*
One-way coupled	Active	Active	*One-way coupled*	0.26	2.40
Two-way coupled			*Two-way coupled*	27.12	30.14
Optimization time (s)	*Aggr.*	*Non-Aggr.*	**Optimization iterations**	*Aggr.*	*Non-Aggr.*
One-way coupled	23.0	61.5	*One-way coupled*	72	26
Two-way coupled	2163.8	760.0	*Two-way coupled*	80	26

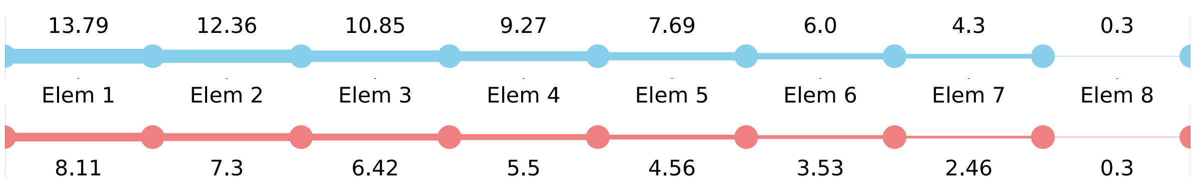

Fig. 13 Optimized thickness (mm) of top and bottom skin panels of initial design

After the aeroelastic optimization studies, the most important conclusions concerning the full-scale MDO problem are as follows.

1) We will only consider one-way coupling due to the significant (two orders of magnitude) decrease in optimization time compared to the two-way coupled case and the negligible effect on the optimized wing mass.
2) We will only consider plate buckling constraints as the stress and displacement constraints are largely inactive.
3) We will not aggregate the plate buckling constraints to avoid potential conditioning issues using the KS function.

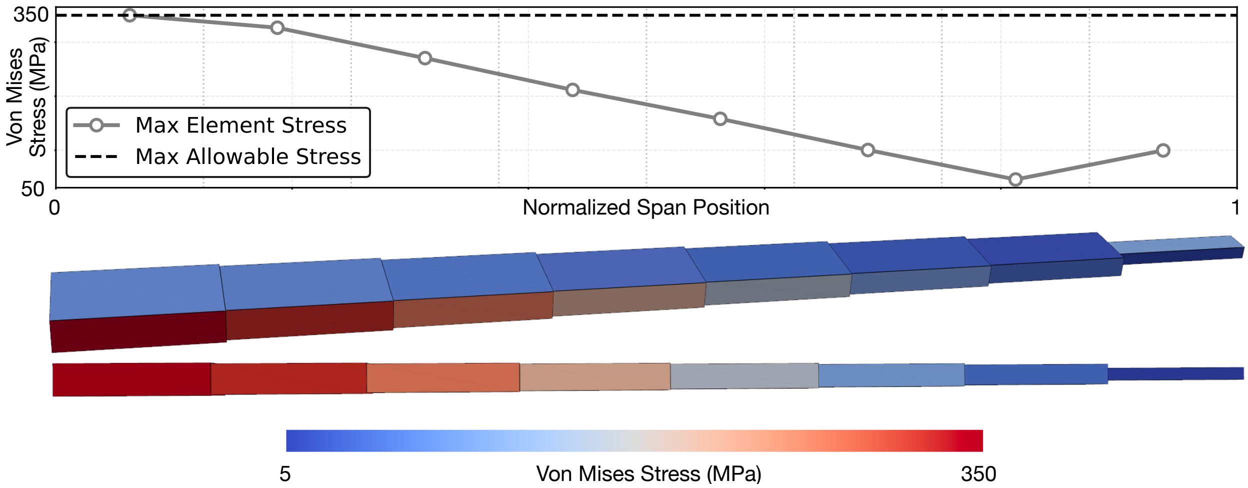

Fig. 14 Optimized beam stress distribution of initial design

B. Full-Scale MDO Problem

The full-scale MDO problem combines all subproblems in Table 2 into a single monolithic problem. Table 6 provides a detailed breakdown of the design variables and constraints. The design variables can be loosely grouped into planform variables (e.g., wing area, rotor chord profile), trim variables (e.g., rotor speed, aircraft pitch), material thickness variables, and powertrain variables (battery mass and motor lengths). Regarding optimization constraints, we enforce aircraft trim (i.e., force and moment balance) in the various mission segments and prescribe an acceleration profile during the quasi-steady transition. In addition to aircraft trim, we enforce static longitudinal stability with an 8% static margin (SM) constraint, normalized by the mean aerodynamic chord (MAC).

Regarding the noise footprint, we impose an acoustic constraint in hover requiring the A-weighted sound pressure level to not exceed 70 dBA, evaluated at a 45° observer angle and an observer distance of 100 m. We note that this single constraint does not fully represent community noise exposure, as the noise field depends on the relative observer position. Observers near the rotor disk plane (e.g., during ground operations) are exposed predominantly to tonal noise, whereas observers located out of plane (e.g., beneath the aircraft in hover) experience primarily broadband noise. A more comprehensive assessment of community noise exposure would therefore require multiple acoustic constraints across relevant observer positions and flight conditions. In this work, we enforce a single constraint due to limited computational resources given the overall high complexity of our computational model. However, the results demonstrate that even a single acoustic constraint has a significant influence on vehicle sizing.

For the powertrain, we enforce a torque safety margin constraint so that each motor can provide at least 10% more torque than the maximum required aerodynamic torque. We also enforce a minimum end-of-mission battery state of charge (SoC) constraint of 20%. This constraint ensures a sufficient voltage margin, as cell voltage declines sharply at low SoC, reducing the battery's ability to deliver the high power required for hover, landing, or go-around maneuvers [119]. Retaining this SoC margin also provides redundancy for contingencies such as unexpected delays, diversions, or emergency operations, while mitigating degradation and extending battery life.

Table 6 Full-scale optimization problem

	Variable/function	Quantity	Variable/function	Quantity
minimize	Aircraft mass			
w.r.t.	aspect ratio (wing/tail)	2	planform area (wing/tail)	2
	fuselage length	1	rotor radius	5
	blade chord (5x4)	20	blade twist (5x4)	20
	battery mass	1	motor length	5
	lift rotor speed		pusher rotor speed	
	hover	4	transition (x5)	5
	transition (5x4)	20	climb, cruise, descent	3
	OEI (4x7)	28	elevator deflection	
	aircraft pitch		transition	5
	climb, cruise, descent, +3g/-1g	5	climb, cruise, descent	3
	front spar thickness	8	rear spar thickness	8
	top skin thickness	8	bottom skin thickness	8
	# design variables	161		
subject to	hover total noise (dBA)	1	static margin	1
	aircraft trim		acceleration	
	hover (F_z, $M_{x,y}$)	3	transition ($\dot{u}$, $\dot{w}$) (5x2)	10
	climb ($F_{x,z}$, M_y)	3	skin plate buckling	14
	cruise ($F_{x,z}$, M_y)	3	final battery SoC	1
	descent ($F_{x,z}$, M_y)	3	radius intersection	2
	transition ($\dot{v}$, $\dot{p}$, $\dot{q}$, $\dot{r}$) (5x4)	20	motor torque safety margin	9
	OEI ($F_{y,z}$, $M_{x,y,z}$) (4x5)	20	hover rotor tip speed ($M_{\text{tip}} \leq 0.6$)	4
	+3g, -1g (F_z)	2		
	# constraints	96		

Having summarized the constraints for the full-scale problem, we report the corresponding values for the baseline and optimized designs in Table 7, with vector-valued constraints indicated in bold. We see that almost all constraints for the baseline and optimized designs are satisfied, with most being active. For the trim constraints (i.e., force and moment equilibrium), we note that although the maximum constraint violations are on the order of 10s of Newton-(meter), these values are negligible compared to the aircraft gross weight, which is three orders of magnitude greater. Therefore, we treat the trim constraints as satisfied. Between the baseline and optimized designs, one notable difference is that skin panel buckling is inactive, and the motor torque safety margin constraint is only partially active in the baseline design, whereas in the optimized design, both constraints are fully active. This result is reasonable since the baseline design (see Sec. II.F) is defined as the feasible design with the least deviation from the initial design, and therefore, the wing and motors do not necessarily need to be as light as possible. For the optimized design, on the other hand, the objective is gross weight, and therefore the aircraft is sized as light as possible while meeting the minimum safety margins. The only constraint that is fully inactive in the baseline and optimized designs is the hover rotor tip speed. This is likely due to the active noise constraint, which indirectly limits rotor tip speed. Lastly, the maximum stress constraint was not enforced in the large-scale MDO problem to improve computational efficiency, as discussed in the the previous section (Sec. V.A). However, we see that as a result, the maximum stress is exceeded at the innermost panel, by about 6% in the baseline design and by about 16% in the optimized design. The detailed stress distribution is shown in Fig. 21 in the appendix. These results indicate that although panel buckling is the primary sizing constraint under the given structural sizing conditions (steady +3g/-1g loads), shear stress cannot be neglected, specifically at the inner part of the wing, and should be constrained in future studies.

Table 7 Constraint values for baseline and optimized designs

Constraint name	**Limit / target**	**Baseline design**			**Optimized design**			**Comment**
		min	*max*	*% viol.*	*min*	*max*	*% viol.*	
Acoustic level (dBA)	$\leq$ 70.00	70.00	70.00	0.00	70.00	70.00	0.00	Active
Aircraft trim (N, N-m)	= **0.00**	1.32×10^{-7}	13.56	0.04	4.56×10^{-8}	25.06	0.06	% viol. w.r.t. $W_0 \sim 10^4$ N
Acceleration (m/s^2)	= $\mathbf{a}_{\text{prescr.}}$	0.17	1.42	1.21	0.17	1.42	0.87	5 quasi-steady transition points (Fig. 11)
Static margin	$\geq$ 0.08	0.08	0.08	0.00	0.08	0.08	0.00	Active
Skin panel buckling	$\leq$ **1.00**	0.15	0.61	0.00	1.00	1.00	0.00	Inactive in baseline
Max. stress (MPa)	$\leq$ **350.00**	4.67	372.70	6.53	9.35	406.17	16.04	Violation at innermost shear panel only
Final battery SoC	$\geq$ 0.20	0.20	0.20	0.00	0.20	0.20	0.00	Active
Motor torque safety margin	$\geq$ **0.10**	0.10	0.54	0.00	0.10	0.10	0.00	Partially inactive in baseline
Rotor intersection (m)	= **0.20**	0.20	0.20	0.00	0.20	0.20	0.00	Active
Hover rotor tip speed	$\leq$ **0.60**	0.45	0.47	0.00	0.45	0.46	0.00	Inactive

Next, we compare two sets of results—one with the static margin constraint and one without—to investigate the effect of enforcing static stability on the optimized design. In the initial sizing of the lift-plus-cruise reference vehicle (see, Silva et al. [116]), static stability was not explicitly enforced. Our results show that static margin, as expected, has a significant impact on the optimized design, and we will discuss the main differences in the optimization results next. In addition, the two sets of results demonstrate the flexibility of our MDO framework for aircraft conceptual design. In Table 8, we show several high-level geometric planform variables as well as the gross weight for the initial, baseline, and optimized designs. Figure 15 shows the design changes from a top-down view.

Table 8 High-level geometric variables and gross mass for initial, baseline, and optimized designs

Design	$\boldsymbol{l}_{\textbf{fuselage}}$ (m)	$\boldsymbol{S}_{\textbf{ref, wing}}$ (m^2)	$\textbf{AR}_{\textbf{wing}}$	$\boldsymbol{S}_{\textbf{ref, tail}}$ (m^2)	$\textbf{AR}_{\textbf{tail}}$	$\boldsymbol{R}_{\textbf{pusher}}$ (m)	$\boldsymbol{R}_{\textbf{lift, 1}}$ (m)	$\boldsymbol{R}_{\textbf{lift, 2}}$ (m)	$\boldsymbol{W_0}$ (kg)
Initial	9.14	19.60	12.12	3.70	4.30	1.37	1.52	1.52	3723.99
Baseline w/o SM	8.81	19.35	12.24	3.70	4.30	1.37	1.54	1.54	3846.90
Optimized w/o SM	8.72	15.04	15.76	2.59	3.01	1.78	1.65	1.42	3601.95
Baseline w/ SM	10.64	17.65	13.30	3.64	4.27	1.38	1.51	1.55	4077.36
Optimized w/ SM	10.66	15.04	15.76	2.59	3.01	1.78	1.47	1.60	3814.75

When the static margin constraint is enforced, the most noticeable geometric change compared to the initial reference

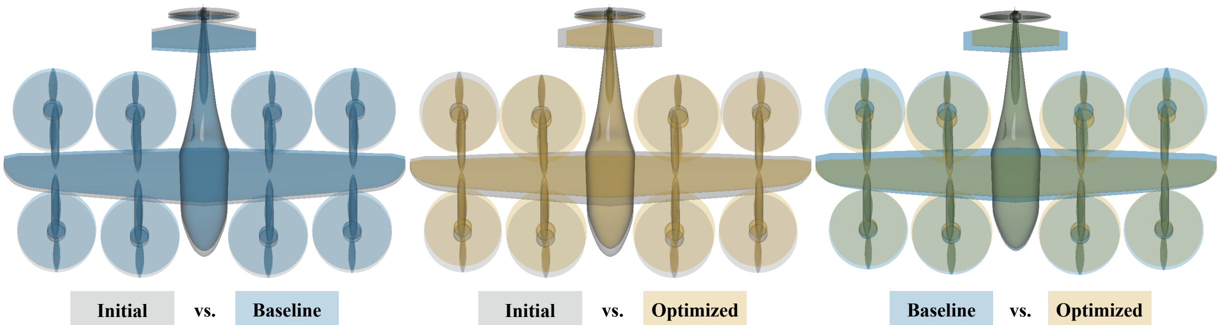

(a) Without static margin constraint

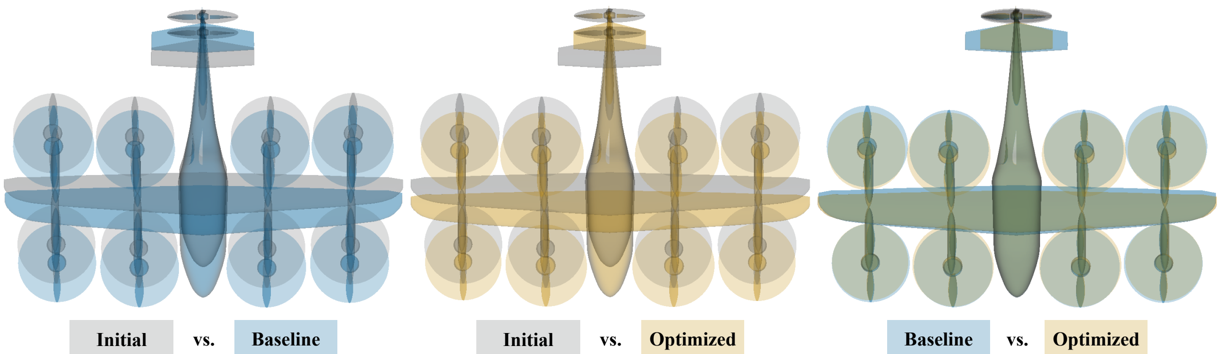

(b) With static margin constraint

Fig. 15 Planform geometry comparison between initial, baseline, and optimized designs

design is an elongated fuselage (16.5% longer), as highlighted in Fig. 15b. This result aligns with engineering intuition, since static margin is a measure of longitudinal stability, and increasing fuselage length increases the tail moment arm, thereby improving control authority. Notably, both the baseline and optimized designs exhibit elongated fuselages. We recall that the baseline design (see Sec. II.F) represents the design with the smallest deviation from the initial reference design while satisfying all constraints, indicating that the initial reference design, based on our computational model, is not feasible with respect to a static margin requirement of 8%.

Extending the fuselage to improve control authority incurs a significant gross weight penalty. Relative to the initial reference design, the optimized configuration is 2.4% heavier (or 6.5% heavier than the baseline). Conversely, without the static margin constraint, the optimized design is approximately 3.3% lighter than the initial reference design (or 6.4% lighter than the baseline). Thus, enforcing the static margin constraint increases the gross weight by roughly 6%. A detailed mass breakdown is provided in Fig. 19 and Fig. 20 in the Appendix.

Next, we examine how coupling between disciplines contributes to the observed weight increase. As implied above, the stability and weights disciplines are tightly coupled since the static margin constraint leads to a longer and significantly heavier (28%) fuselage. However, in Table 8, we see that other planform variables such as reference areas and aspect ratios for the wing and tail converged to the same values when comparing the optimized designs. These values correspond to the upper and lower design variable bounds. This suggests coupling between other disciplines plays an important role in the aircraft's sizing.

Figure 16 reveals additional effects of the static margin constraint on aircraft sizing and performance. The motor mass increases substantially (by ~23%), consistent with the power demand profile shown in Fig. 16b. Power during hover and transition is more than 20% higher, on average, when the static margin constraint is enforced. Since induced power in hover scales with gross weight as $P_i \propto W_0^{3/2}$, and the gross weight only increases by about 6%, the expected power increase based solely on weight would be approximately 9%—far less than observed. The larger power increase is primarily due to the acoustic constraint, which drives the design toward a less aerodynamically efficient rotor blade. Figure 16a shows that the mean figure of merit of the lift rotors in hover decreases by more than 10% when static margin is enforced. This result is consistent with findings from a previous study [52], where we investigated the tradeoff between rotor noise and rotor-aerodynamic efficiency. The loss in aerodynamic efficiency explains the higher hover and transition power, as well as the corresponding increase in motor mass.

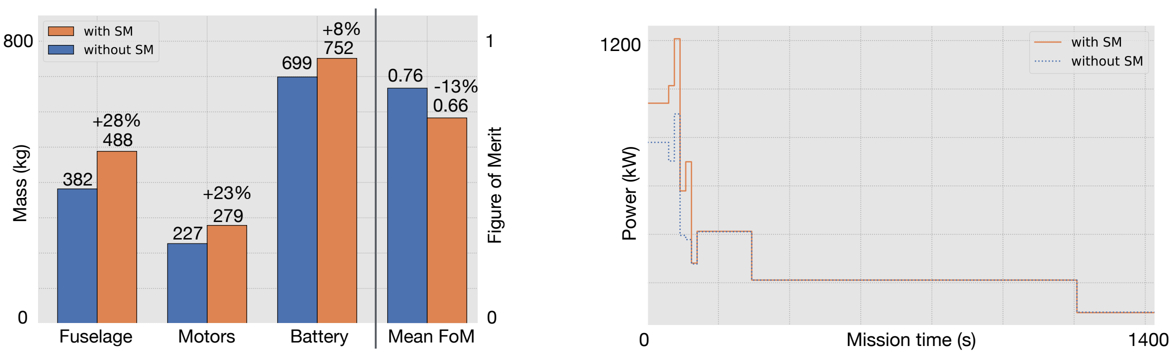

(a) Component mass and figure of merit comparison **(b) Power profile comparison**

Fig. 16 Impact of static margin on aircraft sizing and performance

In summary, enforcing a static margin constraint elongates the fuselage to improve longitudinal control authority, thereby increasing both fuselage and overall vehicle weight. To satisfy the noise constraint of the heavier aircraft, the lift rotors become less aerodynamically efficient, which further increases power demand during hover and transition. This, in turn, necessitates larger and heavier motors, compounding the overall increase in vehicle gross weight.

C. Parameter Sweeps

In this section, we present a set of parameter sweeps whose results are shown in Fig. 17, where each point represents the result of a converged full-scale optimization. In Fig. 17a, we vary the battery energy density from 250 to 450 Wh/kg. The initial design was sized by NASA [116] with an energy density of 400 Wh/kg. Our results agree qualitatively with what is expected, showing a nonlinear inverse relationship between gross weight and energy density. This highlights the importance of future improvements in battery technology. In addition to varying the battery energy density, we also investigate the effect of increasing the final state-of-charge (SoC) constraint from 0.1 to 0.3. For the initial design, this constraint was set to 0.2 (see [116]). The results, shown in Fig. 17b, indicate a mostly linear relationship between gross weight and final SoC, which also agrees qualitatively with what is expected. In both plots, we indicate the baseline design with a star-shaped marker to emphasize the impact of large-scale MDO. Because the initial design is defined for a single battery energy density and final SoC, we only compute the baseline design for this specific combination.

Figure 18 presents similar parameter sweeps, this time comparing results from the full-scale MDO problem with and without the static margin constraint. When the static margin constraint is omitted, the trends remain similar but show a nearly constant offset, with the optimized designs being, on average, 4.6% lighter in the energy density sweep and 4.8% lighter in the state-of-charge sweep. As discussed earlier (see Fig. 15b), the most notable design difference when enforcing static stability is a longer fuselage, which improves longitudinal control authority. Overall, these parameter sweeps highlight the robustness of our computational approach for solving different optimization problems.

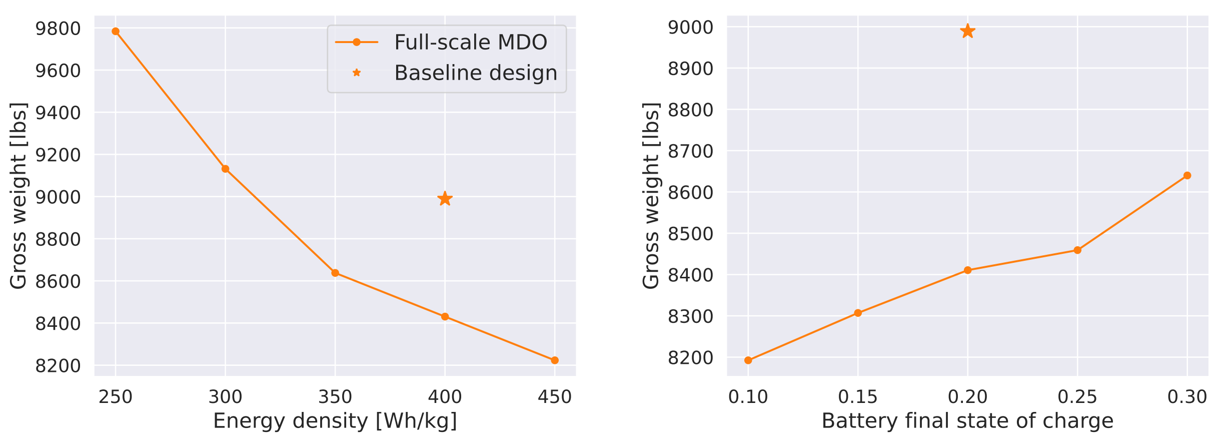

(a) Gross weight vs. energy density **(b) Gross weight vs. SoC**

Fig. 17 Sensitivity of the full-scale MDO solution to battery energy density and final state of charge. The baseline design is shown for comparison.

D. Statistics of Optimization and Computational Model

Lastly, Table 9 summarizes key statistics of the computational model and optimization process for each (sub)-problem, including optimization time, compilation time, total number of graph nodes, memory usage, and other relevant metrics. All results were obtained using a standard desktop computer with an Intel i7 processor (20 cores) and 64 gigabytes (GB) of memory. The operating system was Linux (Ubuntu). On average, the full-scale problem converges in about 50 major optimization iterations, requiring a little over one hour. Subproblems 2, 3, and 4 converge rapidly, requiring less than three minutes to converge, while subproblem 1 takes about 30 minutes. In addition to the optimization time, the

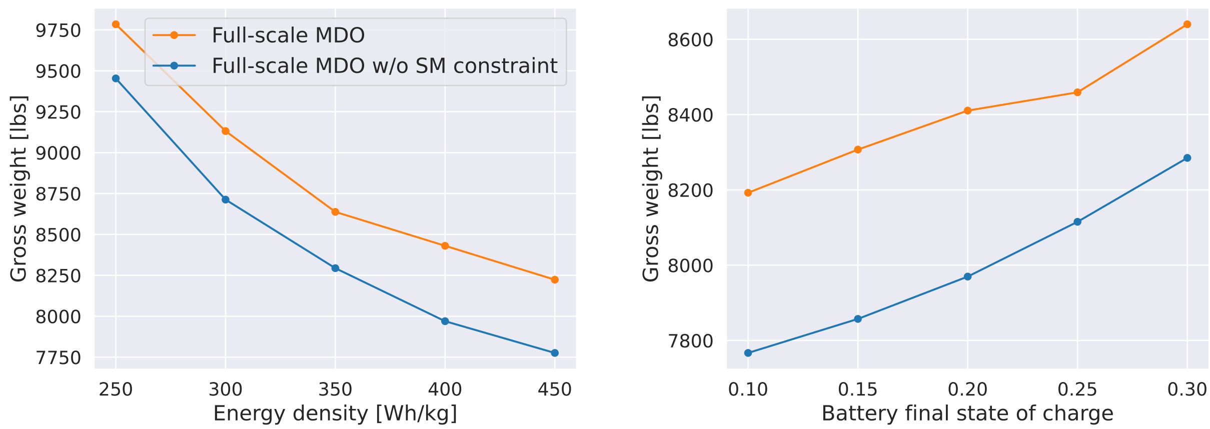

(a) Gross weight vs. battery energy density

(b) Gross weight vs. SoC

Fig. 18 Impact of static margin (SM) on sensitivity of full-scale MDO solution

compilation time is significant, especially for the full-scale problem, which takes about 3.7 hours to compile. The main reason for the long compilation time is that CSDL (see, Sec. II.A) has a non-native performance backend (JAX) that uses the Accelerated Linear Algebra (XLA) compiler for fast execution of the CSDL code. The computational overhead of translating CSDL code into JAX is significant and future versions of CSDL will have a native performance backend to avoid this issue. However, we note that once compiled, the problem can be resolved with different model parameters. That means that to generate the parameter sweeps shown in Fig. 18, we only need to compile each subproblem and the full-scale problem once, leading to a total time of about 37.3 hours (1.6 days) for 20 optimizations. These results suggest that the application of large-scale MDO to aircraft conceptual design of novel aircraft can accelerate the exploration of the design space, especially when considering the use of supercomputing resources, which is an area of future work.

Aside from the optimization and compilation times, a noteworthy statistic is the number of implicit operations. This represents the number of (implicit) residual equations that are computed in the various discipline models (see Table 1). For the full-scale problem, there are 91 implicit operations. The use of the graph-based modeling language CSDL (see Sec. II.A) allows us to efficiently compute the sensitivities of these implicit residuals by the use of the adjoint method, whose computational cost is independent of the number of state variables.

E. Limitations of Results

For conceptual design, the results obtained with the present framework represent a meaningful step forward in terms of model complexity and scope of analysis. Nevertheless, several important drivers of vehicle sizing remain unrepresented because of the simplified mission profile and limitations of the underlying physics-based models. Below is a non-exhaustive summary.

For eVTOL vehicles, a critical analysis missing in this study is the thermal response of the electric powertrain [120].

Table 9 Summary of key statistics of computational model and optimization

Metric	Subproblem 1 (Battery & rotors)	Subproblem 2 (Motors)	Subproblem 3 (Structures)	Subproblem 4 (Planform)	Full-scale problem
Mean optimization time (s)	1839.79	51.05	10.68	142.17	3792.09
Mean major optimization iterations	115.64	29.55	15.45	14.50	49.37
Total graph nodes	354752	85553	122981	177781	721046
Total implicit operations	74	9	4	11	91
Mean compilation time (s)	2735.14	54.68	137.02	914.91	13578.78
Mean forward run time (s)	1.62	0.58	0.06	4.07	7.06
Mean derivative time (s)	5.40	0.32	0.58	5.38	24.84
Approximate memory usage (GB)	9.60	3.50	4.70	12.00	22.60

Heat generated by electric motors and batteries during high-power mission segments such as hover and transition is not directly dissipated to the atmosphere, unlike in conventional aircraft. Because the current motor and battery models do not predict heat generation, the impact of thermal management on gross weight is not captured. Incorporating even low-order thermal models would likely increase the vehicle gross weight (see e.g., [121]).

The simplified mission profile also omits the inbound transition and vertical descent phases. These regimes are dominated by complex flow phenomena, including rotor–rotor and rotor–wing interference, wake re-ingestion, and potential entry into the vortex-ring state [122]. The steady rotor aerodynamic models we employed are not formulated for negative or recirculating inflows, which precludes reliable modeling of these effects. Their omission likely leads to an underprediction of induced power and unsteady loads, biasing the sizing toward a lighter design. In addition, because rotor–rotor and rotor–wing interactions are inherently unsteady, they alter both the instantaneous loading and vortex-wake geometry, which in turn modifies tonal and broadband acoustic sources. The lowest level of fidelity required to capture some of these phenomena would be an unsteady VLM (i.e., free-wake) model (see e.g., [123]). In light of the shortcomings of the aerodynamic models used in this study, we intentionally selected the lift-plus-cruise concept whose geometry reduces sensitivity to rotor–rotor and rotor–wing interactions. This is because the front rotors are mounted below the wing and the rear rotors are mounted above the wing.

Furthermore, aeroelastic effects are only partially captured. The current structural model employs one-dimensional beam elements and steady aerodynamics. In addition, we did not model two-way coupling between structural deformation and aerodynamic loads in the large-scale MDO study. As a result, unsteady phenomena such as flutter or whirl-flutter are not captured. Inclusion of reduced-order aeroelastic models or frequency-domain flutter analyses [124, 125] would alter the optimal stiffness and planform distributions and likely lead to an increase in vehicle gross weight.

VI. Conclusion

This paper presents a novel demonstration of system-level large-scale multidisciplinary design optimization (MDO) of a lift-plus-cruise Urban Air Mobility (UAM) reference vehicle. We consider a comprehensive set of design conditions

(15 total), comprised of steady nominal mission segments (hover, climb, cruise, descent), a quasi-steady constant-altitude transition, four motor failure conditions, and two static structural sizing conditions. Our system-level computational model integrates several low to mid-fidelity physics-based models for aerodynamics, propulsion, structures, aeroacoustics, motor performance, battery, and static aircraft stability. Where appropriate, semi-empirical models and regressions (e.g., for weight estimation) complement these physics-based models to help size certain subsystems.

Our large-scale MDO problem is a minimization of gross weight of a lift-plus-cruise UAM vehicle. We consider 161 design variables and 96 constraints, spanning all modeled disciplines. Two key enablers allow us to solve this problem efficiently. First, we leverage a recently developed, graph-based modeling language that fully automates adjoint-based sensitivity analysis. In addition to reducing the implementation effort, this graph-based modeling language is crucial for efficiently handling the large number (91) of implicit residual equations in our computational model. Second, we use a warm-starting procedure that solves four optimization subproblems, each sizing individual subsystems and converging rapidly. This provides a good initial guess and appropriate design variable scaling for the large-scale MDO problem, which is critical for reliable convergence of the proposed MDO approach for vehicle design.

One of the optimization subproblems is an aeroelastic optimization aimed at sizing the wing box. We consider stress, displacement, and plate buckling constraints in an aggregated and non-aggregated manner, and investigate the effect of resolving the aeroelastic coupling. Our findings indicate that the wing structure is primarily sized by the plate buckling constraint. In addition, resolving the aeroelastic coupling increases the optimization time by two orders of magnitude with a negligible impact on the optimized design (0.1% difference in terms of structural wing mass). Constraint aggregation results in a reduction of total optimization time but an increase in optimization iterations. These results inform our strategy for the structures discipline in the large-scale MDO problem (i.e., gross weight minimization), where we omit the stress and displacement constraints and only consider one-way aeroelastic coupling, neglecting the effect of the structural displacement on the aerodynamic solution. For the full-scale problem, we consider two variants of the gross weight minimization: one with a static margin (SM) stability constraint and one without it. In both cases, we find that large-scale MDO leads to a decrease in gross weight of about 6.5% compared to the respective baseline design with all optimization constraints being satisfied. However, when enforcing the SM constraint, the optimized vehicle is about 5.9% heavier compared to the optimized design without the SM constraint. This increase in gross weight is primarily due to a significant elongation of the fuselage for increased control authority. We demonstrate the effectiveness of our approach through a set of parameter sweeps (a total of 20 optimizations) where we vary the battery energy density and the end-of-mission battery state of charge. The results align with engineering intuition, showing an inverse relationship between gross weight and battery energy density, and a linear relationship between gross weight and end-of-mission state of charge. Using standard computing resources, the total time to generate all results is less than two days.

The results of this study demonstrate the potential of accelerating aircraft conceptual design through system-level, large-scale MDO. However, several limitations remain, leaving significant room for future work. First, the modeling fidelity of our physics-based models is insufficient to account for important interactions between subsystems. In particular, we emphasize the aerodynamics, structures, and power electronics disciplines. For the aerodynamics discipline, a significant improvement would be the use of the vortex panel method instead of the vortex lattice method to model interactions between non-lifting surfaces. Similarly, replacing the beam model with a shell model (e.g., Reissner–Mindlin) would expand the structural modeling capabilities beyond the wing box. In addition, two-way aeroelastic coupling, in which structural displacements affect the aerodynamic solution, would enable the modeling of unsteady aeroelastic phenomena such as flutter. For modeling power electronics, components such as the DC bus and inverters should be explicitly modeled, rather than represented by assumed component efficiencies, and a battery model that takes into account the electrochemistry should be considered instead of an energy-based formulation. Moreover, the thermal response of the powertrain, especially in high-power design conditions like hover, should be modeled. Second, more design conditions should be included that account for transient effects, which play an important role in subsystem sizing. Examples include gust response, inbound transition, or dynamic stability conditions. Similarly, incorporating more optimization constraints like handling qualities or multiple (rather than a single) acoustic constraints to better represent community noise exposure, would lead to a more well-rounded design. Third, to improve the initial guess and scaling of our large-scale MDO problem , the warm-starting sequence can be refined by considering the coupling between the smaller optimization subproblems . This can be done by iteratively solving the sequence of optimization subproblems , for example, via a block coordinate optimization algorithm. The added cost would be manageable due to the small computational cost of the subproblems compared to the full-scale problem. Fourth, applying our approach to other UAM concepts, such as a tilt-rotor configuration, would further demonstrate the potential of system-level large-scale MDO in the design of novel aircraft concepts.

Appendix

A. Supplementary Equations

The set of rigid-body six-degrees-of-freedom equations of motion are given as

$$X - mg\sin\theta = m\left(\dot{u} + qw - rv\right) \tag{34a}$$

$$Y + mg\cos\theta\sin\phi = m\left(\dot{v} + ru - pw\right) \tag{34b}$$

$$Z + mg\cos\theta\cos\phi = m\left(\dot{w} + pv - qu\right) \tag{34c}$$

$$L = I_x\dot{p} - I_{yz}\left(q^2 - r^2\right) - I_{zx}\left(\dot{r} + pq\right) - I_{xy}\left(\dot{q} - rp\right) - \left(I_y - I_z\right)qr \tag{34d}$$

$$M = I_y\dot{q} - I_{zx}\left(r^2 - p^2\right) - I_{xy}\left(\dot{p} + qr\right) - I_{yz}\left(\dot{r} - pq\right) - \left(I_z - I_x\right)rp \tag{34e}$$

$$N = I_z\dot{r} - I_{xy}\left(p^2 - q^2\right) - I_{yz}\left(\dot{q} + rp\right) - I_{zx}\left(\dot{p} - qr\right) - \left(I_x - I_y\right)pq, \tag{34f}$$

where the total forces about the x-, y-, and z-axis are represented as X, Y, Z, respectively; total moments about these axes as L, M, and N; linear velocity as u, v, and w; rotational velocity as p, q, and r; angles of rotations (i.e. Euler angles) ϕ, θ, and ψ.

B. Supplementary Figures

Figures 19 and 20 show a more detailed breakdown of the vehicle gross weight for the baseline and optimized designs with and without the static margin constraint. Figure 21 shows the beam stress distribution for the optimized design of the full-scale MDO study (no stress constraint), highlighting the violation of the stress constraint at the innermost shear panel.

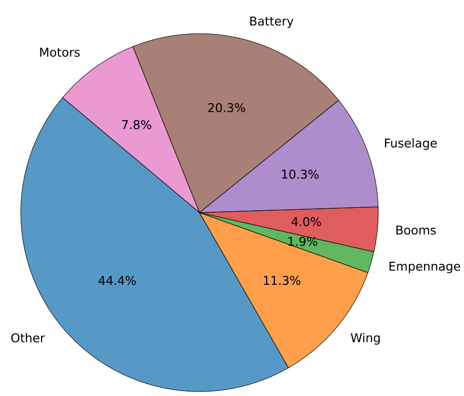

(a) Baseline design

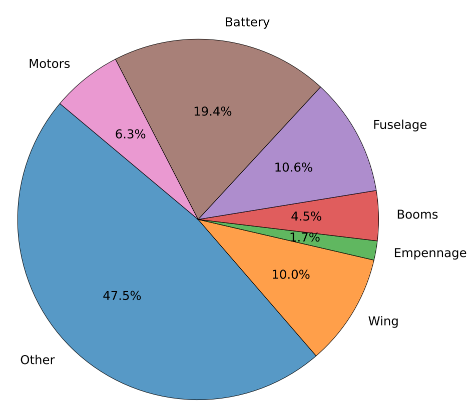

(b) Optimized design

Fig. 19 Mass breakdown without static margin constraint

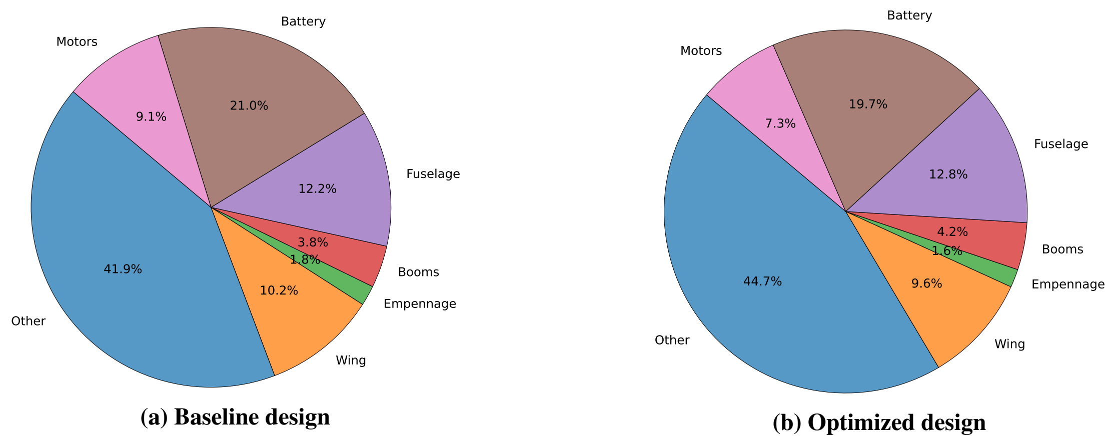

Fig. 20 Mass breakdown with static margin constraint

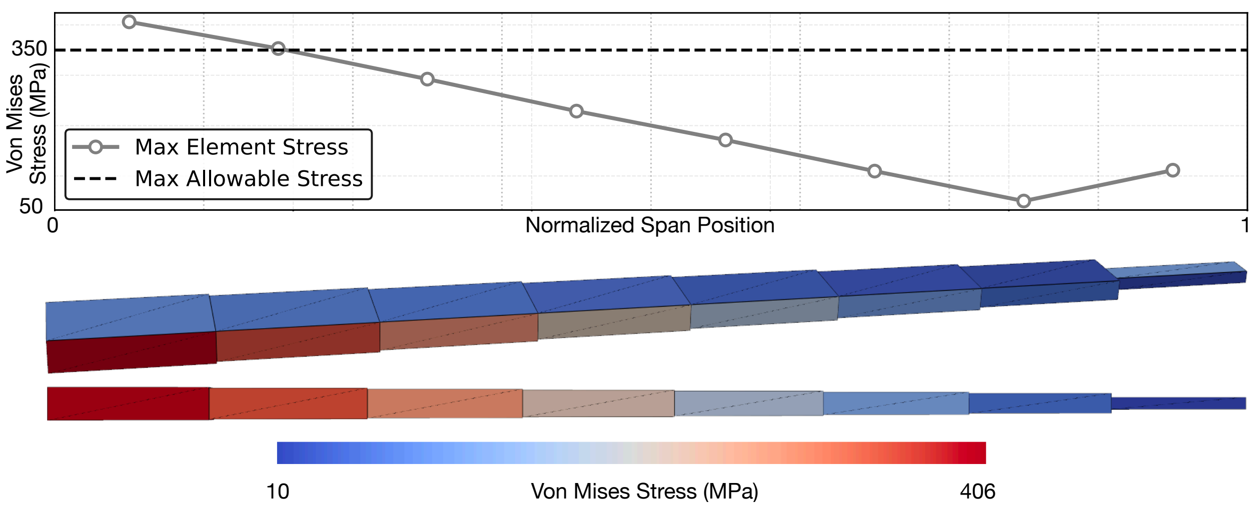

Fig. 21 Beam stress distribution after the full-scale MDO

Funding Sources

The material presented in this paper is supported, in part, by NASA under award No. 80NSSC21M0070.

Acknowledgments

The authors acknowledge the use of generative AI (ChatGPT) in proofreading this manuscript.

References

[1] Thipphavong, D. P., Apaza, R., Barmore, B., Battiste, V., Burian, B., Dao, Q., Feary, M., Go, S., Goodrich, K. H., Homola, J., et al., "Urban Air Mobility Airspace Integration Concepts and Considerations," *2018 Aviation Technology, Integration, and Operations Conference*, AIAA, 2018, p. 3676. https://doi.org/10.2514/6.2018-3676.

[2] Raymer, D., *Aircraft Design: A Conceptual Approach, Fifth Edition*, AIAA, 2012. https://doi.org/10.2514/4.869112.

[3] Roskam, J., *Airplane Design Parts I Through VIII*, 2nd ed., DARcorporation, Lawrence, Kansas, 2003.

[4] Torenbeek, E., *Synthesis of Subsonic Airplane Design: An Introduction to the Preliminary Design of Subsonic General Aviation and Transport Aircraft, with Emphasis on Layout, Aerodynamic Design, Propulsion and Performance*, Springer Science & Business Media, 2013.

[5] McCullers, L., "Aircraft Configuration Optimization Including Optimized Flight Profiles," *NASA. Langley Research Center Recent Experiences in Multidisciplinary Analysis and Optimization, Part 1*, 1984.

[6] Nagel, B., Böhnke, D., Gollnick, V., Schmollgruber, P., Rizzi, A., La Rocca, G., and Alonso, J. J., "Communication in Aircraft Design: Can We Establish a Common Language," *28th International Congress of the Aeronautical Sciences*, Vol. 201, 2012.

[7] Johnson, W., "NDARC: NASA Design and Analysis of Rotorcraft," Technical Publication TP 2015-218751, NASA, Apr. 2015.

[8] De Vries, R., Hoogreef, M. F., and Vos, R., "Range Equation for Hybrid-Electric Aircraft With Constant Power Split," *Journal of Aircraft*, Vol. 57, No. 3, 2020, pp. 552–557. https://doi.org/10.2514/1.c035734.

[9] Finger, D. F., de Vries, R., Vos, R., Braun, C., and Bil, C., "A Comparison of Hybrid-Electric Aircraft Sizing Methods," *AIAA SciTech 2020 Forum*, AIAA, 2020, p. 1006. https://doi.org/10.2514/6.2020-1006.

[10] Chakraborty, I., and Mishra, A. A., "Generalized Energy-Based Flight Vehicle Sizing and Performance Analysis Methodology," *Journal of Aircraft*, Vol. 58, No. 4, 2021, pp. 762–780. https://doi.org/10.2514/1.c036101.

[11] Finger, D. F., Bil, C., and Braun, C., "Initial Sizing Methodology for Hybrid-Electric General Aviation Aircraft," *Journal of Aircraft*, Vol. 57, No. 2, 2020, pp. 245–255. https://doi.org/10.2514/1.c035428.

[12] Hu, J., and Booker, J., "Preliminary Sizing of Electric-Propulsion Powertrains for Concept Aircraft Designs," *Designs*, Vol. 6, No. 5, 2022, p. 94. https://doi.org/10.3390/designs6050094.

[13] Park, J., Lee, D., Lim, D., and Yee, K., "A Refined Sizing Method of Fuel Cell–Battery Hybrid System for eVTOL Aircraft," *Applied Energy*, Vol. 328, 2022, p. 120160. https://doi.org/10.1016/j.apenergy.2022.120160.

[14] Swaminathan, N., Reddy, S. R. P., RajaShekara, K., and Haran, K. S., "Flying Cars and eVTOLs—Technology Advancements, Powertrain Architectures, and Design," *IEEE Transactions on Transportation Electrification*, Vol. 8, No. 4, 2022, pp. 4105–4117. https://doi.org/10.1109/tte.2022.3172960.

[15] Verstraete, D., Lehmkuehler, K., Gong, A., Harvey, J. R., Brian, G., and Palmer, J. L., "Characterisation of a Hybrid, Fuel-Cell-Based Propulsion System for Small Unmanned Aircraft," *Journal of Power Sources*, Vol. 250, 2014, pp. 204–211. https://doi.org/10.1016/j.jpowsour.2013.11.017.

[16] Chauhan, S. S., and Martins, J. R., "Tilt-Wing eVTOL Takeoff Trajectory Optimization," *Journal of Aircraft*, Vol. 57, No. 1, 2020, pp. 93–112. https://doi.org/10.2514/1.c035476.

[17] Wang, M., Diepolder, J., Zhang, S., Söpper, M., and Holzapfel, F., "Trajectory Optimization-Based Maneuverability Assessment of eVTOL Aircraft," *Aerospace Science and Technology*, Vol. 117, 2021, p. 106903. https://doi.org/10.1016/j.ast.2021.106903.

[18] Pradeep, P., Lauderdale, T. A., Chatterji, G. B., Sheth, K., Lai, C. F., Sridhar, B., Edholm, K.-M., and Erzberger, H., "Wind-Optimal Trajectories for Multirotor eVTOL Aircraft on UAM Missions," *AIAA AVIATION 2020 Forum*, AIAA, 2020, p. 3271. https://doi.org/10.2514/6.2020-3271.

[19] Tagg, A. C., Joseph, C., Anderson, R., Green, E., and Ning, A., "Trajectory Optimization of eVTOL and Conventional Aircraft: A Comparative Analysis of Vortex Particle Method and Vortex Lattice + Blade Element Momentum Theory," *AIAA AVIATION Forum and ASCEND 2024*, AIAA, 2024, p. 3587. https://doi.org/10.2514/6.2024-3587.

[20] Yeh, S.-T., and Du, X., "Optimal Tilt-Wing eVTOL Takeoff Trajectory Prediction Using Regression Generative Adversarial Networks," *Mathematics*, Vol. 12, No. 1, 2023, p. 26. https://doi.org/10.3390/math12010026.

[21] Orndorff, N. C., and Hwang, J. T., "Air-Taxi Trajectory Optimization with Aerodynamic and Motor Models," *arXiv preprint arXiv:2404.15570*, 2024. https://doi.org/https://doi.org/10.48550/arXiv.2404.15570.

[22] Orndorff, N. C., Sarojini, D., Scotzniovsky, L., Gill, H., Lee, S., Cheng, Z., Zhao, S., Mi, C., and Hwang, J. T., "Air-taxi transition trajectory optimization with physics-based models," *AIAA SCITECH 2023 Forum*, AIAA, 2023, p. 0324. https://doi.org/10.2514/6.2023-0324.

[23] Kaneko, S., and Martins, J. R., "Simultaneous Design and Trajectory Optimization Strategies for Computationally Expensive Models," *AIAA Journal*, 2025, pp. 1–19. https://doi.org/10.2514/1.j063976.

[24] Gill, H., Lee, S., Ruh, M. L., and Hwang, J. T., "Applicability of Low-Fidelity Tonal and Broadband Noise Models on Small-Scale Rotors," *AIAA SCITECH 2023 Forum*, AIAA, 2023. https://doi.org/10.2514/6.2023-1547.

[25] Gill, H., and Lee, S., "Development of New Empirical Rotor Broadband Noise Prediction Models for Urban Air Mobility Applications," *AIAA SCITECH 2024 Forum*, AIAA, 2024. https://doi.org/10.2514/6.2024-2473.

[26] Weitsman, D., and Greenwood, E., "Parametric Study of eVTOL Rotor Acoustic Design Trades," *AIAA Scitech 2021 Forum*, AIAA, 2021, p. 1987. https://doi.org/10.2514/6.2021-1987.

[27] Clarke, M. A., and Alonso, J., "Evaluating the Performance and Acoustic Footprint of Aircraft for Regional and Urban Air Mobility," *AIAA Aviation 2021 Forum*, AIAA, 2021, p. 3205. https://doi.org/10.2514/6.2021-3205.

[28] Li, S., and Lee, S., "UCD-QuietFly: A New Program to Predict Multi-Rotor eVTOL Broadband Noise," *2020 VFS Aeromechanics for Advanced Vertical Flight Technical Meeting*, Vertical Flight Society, Fairfax, VA, 2020.

[29] Clarke, M. A., and Botero, E., "Aeroacoustic Optimization of VTOL Rotor Blades," *AIAA SCITECH 2023 Forum*, AIAA, 2023, p. 0209. https://doi.org/10.2514/6.2023-0209.

[30] Pacini, B., Yildirim, A., Davoudi, B., Martins, J. R., and Duraisamy, K., "Towards Efficient Aerodynamic and Aeroacoustic Optimization for Urban Air Mobility Vehicle Design," *AIAA AVIATION 2021 Forum*, AIAA, 2021, p. 3026. https://doi.org/10.2514/6.2021-3026.

[31] Ingraham, D., Gray, J. S., and Lopes, L. V., "Gradient-Based Propeller Optimization with Acoustic Constraints," *AIAA Scitech 2019 Forum*, AIAA, 2019. https://doi.org/10.2514/6.2019-1219.

[32] Stokkermans, T. C., Usai, D., Sinnige, T., and Veldhuis, L. L., "Aerodynamic Interaction Effects Between Propellers in Typical eVTOL Vehicle Configurations," *Journal of Aircraft*, Vol. 58, No. 4, 2021, pp. 815–833. https://doi.org/10.2514/1.c035814.

[33] Piccinini, R., Tugnoli, M., and Zanotti, A., "Numerical Investigation of the Rotor–Rotor Aerodynamic Interaction for eVTOL Aircraft Configurations," *Energies*, Vol. 13, No. 22, 2020, p. 5995. https://doi.org/10.3390/en13225995.

[34] Zanotti, A., and Algarotti, D., "Aerodynamic Interaction Between Tandem Overlapping Propellers in eVTOL Airplane Mode Flight Condition," *Aerospace Science and Technology*, Vol. 124, 2022, p. 107518. https://doi.org/10.1016/j.ast.2022.107518.

[35] Caprace, D.-G., Ning, A., Chatelain, P., and Winckelmans, G., "Effects of Rotor–Airframe Interaction on the Aeromechanics and Wake of a Quadcopter in Forward Flight," *Aerospace Science and Technology*, Vol. 130, 2022, p. 107899. https://doi.org/10.1016/j.ast.2022.107899.

[36] Chang, M., Zheng, Z., Meng, X., Bai, J., and Wang, B., "Aerodynamic Analysis of a Low-Speed Tandem-Channel Wing for eVTOL Aircraft Considering Propeller–Wing Interaction," *Energies*, Vol. 15, No. 22, 2022, p. 8616. https://doi.org/10.3390/en15228616.

[37] Lee, H., Sengupta, B., Araghizadeh, M., and Myong, R., "Review of Vortex Methods for Rotor Aerodynamics and Wake Dynamics," *Advances in Aerodynamics*, Vol. 4, No. 1, 2022, p. 20. https://doi.org/10.1186/s42774-022-00111-3.

[38] Bacchini, A., Cestino, E., Van Magill, B., and Verstraete, D., "Impact of Lift Propeller Drag on the Performance of eVTOL Lift+Cruise Aircraft," *Aerospace Science and Technology*, Vol. 109, 2021, p. 106429. https://doi.org/10.1016/j.ast.2020.106429.

[39] Riboldi, C. E., Gualdoni, F., and Trainelli, L., "Preliminary Weight Sizing of Light Pure-Electric and Hybrid-Electric Aircraft," *Transportation Research Procedia*, Vol. 29, 2018, pp. 376–389. https://doi.org/10.1016/j.trpro.2018.02.034.

[40] Winter, T. F., Robinson, J., Gamez, A., and Nascenzi, T., "Conceptual Design Structural Sizing for Urban Air Mobility," *AIAA SciTech 2021 Forum*, AIAA, 2021, p. 1722. https://doi.org/10.2514/6.2021-1722.

[41] Nascenzi, T., Cuatt, T., Winter, T. F., Ruh, M. L., Sarojini, D., Hwang, J. T., and Kiani, S., "Physics-Based Surrogate Models for UAM Weight Prediction," *AIAA SciTech 2023 Forum*, AIAA, 2023, p. 1360. https://doi.org/10.2514/6.2023-1360.

[42] Pacini, B., Prajapati, M., Duraisamy, K., Martins, J. R., and He, P., "Towards Aerostructural Optimization for Urban Air Mobility Vehicle Design," *AIAA SCITECH 2023 Forum*, AIAA, 2023, p. 0326. https://doi.org/10.2514/6.2023-0326.

[43] Koch, C., "Parametric Whirl Flutter Study Using Different Modelling Approaches," *CEAS Aeronautical Journal*, Vol. 13, No. 1, 2022, pp. 57–67. https://doi.org/10.1007/s13272-021-00548-0.

[44] Wright, S. J., "Fundamental Aeroelastic Analysis of an Urban Air Mobility Rotor," *9th Biennial Autonomous VTOL Technical Meeting*, 2021.

[45] Palaia, G., Zanetti, D., Salem, K. A., Cipolla, V., and Binante, V., "THEA-CODE: A Design Tool for the Conceptual Design of Hybrid-Electric Aircraft with Conventional or Unconventional Airframe Configurations," *Mechanics & Industry*, Vol. 22, 2021, p. 19. https://doi.org/10.1051/meca/2021012.

[46] Palaia, G., Abu Salem, K., Cipolla, V., Binante, V., and Zanetti, D., "A Conceptual Design Methodology for e-VTOL Aircraft for Urban Air Mobility," *Applied Sciences*, Vol. 11, No. 22, 2021, p. 10815. https://doi.org/10.3390/app112210815.

[47] Brown, A., and Harris, W. L., "Vehicle Design and Optimization Model for Urban Air Mobility," *Journal of Aircraft*, Vol. 57, No. 6, 2020, pp. 1003–1013. https://doi.org/10.2514/1.c035756.

[48] Ugwueze, O., Statheros, T., Horri, N., Bromfield, M. A., and Simo, J., "An Efficient and Robust Sizing Method for eVTOL Aircraft Configurations in Conceptual Design," *Aerospace*, Vol. 10, No. 3, 2023, p. 311. https://doi.org/10.3390/aerospace10030311.

[49] Chakraborty, I., and Mishra, A. A., "Sizing and Analysis of a Lift-Plus-Cruise Aircraft with Electrified Propulsion," *Journal of Aircraft*, Vol. 60, No. 3, 2023, pp. 747–765. https://doi.org/10.2514/6.2022-3513.

[50] Riboldi, C. E., "An Optimal Approach to the Preliminary Design of Small Hybrid-Electric Aircraft," *Aerospace Science and Technology*, Vol. 81, 2018, pp. 14–31. https://doi.org/10.1016/j.ast.2018.07.042.

[51] Sarojini, D., Ruh, M. L., Sperry, M., Yan, J., Fletcher, A., Joshy, A. J., Scotzniovsky, L., Ivanov, A., Orndorff, N., Gandarillas, V., Asher, I., Chambers, J., Gill, H., Lee, S., Cheng, Z., Rodriguez, G., Zhao, S., Mi, C., Nascenzi, T., Cuatt, T., Winter, T., Guibert, A., Cronk, A., Kim, A., Meng, S., and Hwang, J. T., "Large-Scale Multidisciplinary Design Optimization of an eVTOL Aircraft Using Comprehensive Analysis," *AIAA SCITECH 2023 Forum*, AIAA, 2023. https://doi.org/10.2514/6.2023-0146.

[52] Ruh, M. L., Sarojini, D., Fletcher, A., Asher, I., and Hwang, J. T., "Large-Scale Multidisciplinary Design Optimization of the NASA Lift-Plus-Cruise Concept Using a Novel Aircraft Design Framework," *arXiv preprint arXiv:2304.14889*, 2023. https://doi.org/https://doi.org/10.48550/arXiv.2304.14889.

[53] Ruh, M. L., Fletcher, A., Sarojini, D., Sperry, M., Yan, J., Scotzniovsky, L., van Schie, S. P., Warner, M., Orndorff, N. C., Xiang, R., Joshy, A. J., Zhao, H., Krokowski, J., Gill, H., Lee, S., Cheng, Z., Cao, Z., Mi, C., Silva, C., Wolfe, L., Chen, J.-S., and Hwang, J. T., "Large-scale multidisciplinary design optimization of a NASA air taxi concept using a comprehensive physics-based system model," *AIAA SCITECH 2024 Forum*, AIAA, 2024, p. 0771. https://doi.org/10.2514/6.2024-0771.

[54] Hwang, J. T., and Ning, A., "Large-Scale Multidisciplinary Optimization of an Electric Aircraft for On-Demand Mobility," *2018 AIAA/ASCE/AHS/ASC Structures, Structural Dynamics, and Materials Conference*, AIAA, 2018, p. 1384. https://doi.org/10.2514/6.2018-1384.

[55] Ha, T. H., Lee, K., and Hwang, J. T., "Large-Scale Multidisciplinary Optimization under Uncertainty for Electric Vertical Takeoff and Landing Aircraft," *AIAA SciTech 2020 Forum*, AIAA, 2020, p. 0904. https://doi.org/10.2514/6.2020-0904.

[56] Orndorff, N. C., Wang, B., Ruh, M. L., Fletcher, A., and Hwang, J. T., "Gradient-based sizing optimization of power-beaming-enabled aircraft," *AIAA AVIATION 2023 Forum*, AIAA, 2023, p. 4019. https://doi.org/10.2514/6.2023-4019.

[57] Lukaczyk, T. W., Wendorff, A. D., Colonno, M., Economon, T. D., Alonso, J. J., Orra, T. H., and Ilario, C., "SUAVE: An Open-Source Environment for Multi-Fidelity Conceptual Vehicle Design," *16th AIAA/ISSMO Multidisciplinary Analysis and Optimization Conference*, AIAA, 2015, p. 3087. https://doi.org/10.2514/6.2015-3087.

[58] Gratz, J., Kirk, J., Recine, C., Jasa, J., Aretskin-Hariton, E., Moore, K., and Marfatia, K., "Aviary: An Open-Source Multidisciplinary Design, Analysis, and Optimization Tool for Modeling Aircraft with Analytic Gradients," *AIAA AVIATION FORUM AND ASCEND 2024*, AIAA, 2024, p. 4219. https://doi.org/10.2514/6.2024-4219.

[59] Welstead, J. R., Caldwell, D., Condotta, R., and Monroe, N., "An Overview of the Layered and Extensible Aircraft Performance System (LEAPS) Development," *2018 AIAA Aerospace Sciences Meeting*, AIAA, 2018, p. 1754. https://doi.org/10.2514/6.2018-1754.

[60] Sharpe, P. D., "AeroSandbox: A Differentiable Framework for Aircraft Design Optimization," Ph.d. thesis, Massachusetts Institute of Technology, Cambridge, MA, 2021. URL https://hdl.handle.net/1721.1/131194.

[61] Saberi, H., Hasbun, M., Hong, J., Yeo, H., and Ormiston, R. A., "Overview of RCAS Capabilities, Validations, and Rotorcraft Applications," *American Helicopter Society 71st Annual Forum, Virginia Beach, VA*, The Vertical Flight Society, 2015. https://doi.org/10.4050/f-0080-2024-1105.

[62] Jia, Z., and Lee, S., "Acoustic Analysis of a Quadrotor eVTOL Design via High-Fidelity Simulations," *25th AIAA/CEAS Aeroacoustics Conference*, AIAA, 2019, p. 2631. https://doi.org/10.2514/6.2019-2631.

[63] Alvarez, E. J., and Ning, A., "High-Fidelity Modeling of Multirotor Aerodynamic Interactions for Aircraft Design," *AIAA Journal*, Vol. 58, No. 10, 2020, pp. 4385–4400. https://doi.org/10.2514/1.j059178.

[64] Hwang, J. T., "A Modular Approach to Large-Scale Design Optimization of Aerospace Systems," *Ph.D. Thesis*, 2015.

[65] Gray, J. S., Hwang, J. T., Martins, J. R., Moore, K. T., and Naylor, B. A., "OpenMDAO: An Open-Source Framework for Multidisciplinary Design, Analysis, and Optimization," *Structural and Multidisciplinary Optimization*, Vol. 59, 2019, pp. 1075–1104. https://doi.org/10.1007/s00158-019-02211-z.

[66] Hwang, J. T., and Martins, J. R., "A Computational Architecture for Coupling Heterogeneous Numerical Models and Computing Coupled Derivatives," *ACM Transactions on Mathematical Software (TOMS)*, Vol. 44, No. 4, 2018, pp. 1–39. https://doi.org/10.1145/3182393.

[67] Gandarillas, V., Joshy, A. J., Sperry, M. Z., Ivanov, A. K., and Hwang, J. T., "A Graph-Based Methodology for Constructing Computational Models that Automates Adjoint-Based Sensitivity Analysis," *Structural and Multidisciplinary Optimization*, Vol. 67, No. 5, 2024, p. 76. https://doi.org/10.1007/s00158-024-03792-0.

[68] Bradbury, J., Frostig, R., Hawkins, P., Johnson, M. J., Leary, C., Maclaurin, D., Necula, G., Paszke, A., VanderPlas, J., Wanderman-Milne, S., and Zhang, Q., "JAX: Composable Transformations of Python+NumPy Programs," , 2018. URL http://github.com/jax-ml/jax.

[69] Sperry, M., Kondap, K., and Hwang, J. T., "Automatic Adjoint Sensitivity Analysis of Models for Large-Scale Multidisciplinary Design Optimization," *AIAA AVIATION 2023 Forum*, 2023, p. 3721. https://doi.org/10.2514/6.2023-3721.

[70] Paszke, A., Gross, S., Massa, F., Lerer, A., Bradbury, J., Chanan, G., Killeen, T., Lin, Z., Gimelshein, N., Antiga, L., et al., "PyTorch: An Imperative Style, High-Performance Deep Learning Library," *Advances in Neural Information Processing Systems*, Vol. 32, 2019.

[71] Braibant, V., and Fleury, C., "Shape Optimal Design Using B-Splines," *Computer Methods in Applied Mechanics and Engineering*, Vol. 44, No. 3, 1984, pp. 247–267. https://doi.org/10.1016/0045-7825(84)90132-4.

[72] Warner, M. A. P., Fletcher, A. H., van Schie, S. P. C., and Hwang, J. T., "A Method for Modular MDO Model Assembly via a Solver Independent Field Representation," *AIAA SciTech 2024 Forum*, 2024. https://doi.org/10.2514/6.2024-1802.

[73] van Schie, S., Warner, M., Fletcher, A., and Hwang, J., "Enforcing Work Conservation in Modular Aeroelastic Coupling for Multidisciplinary Design Optimization," 2024. https://doi.org/10.2514/6.2024-2411.

[74] Logan, D. L., *First Course in the Finite Element Method, Enhanced Edition, SI Version*, Cengage Learning, 2022.

[75] Kennedy, G. J., and Hicken, J. E., "Improved Constraint-Aggregation Methods," *Computer Methods in Applied Mechanics and Engineering*, Vol. 289, 2015, pp. 332–354. https://doi.org/10.1016/j.cma.2015.02.017.

[76] Lambe, A. B., Kennedy, G. J., and Martins, J. R., "An Evaluation of Constraint Aggregation Strategies for Wing Box Mass Minimization," *Structural and Multidisciplinary Optimization*, Vol. 55, 2017, pp. 257–277. https://doi.org/10.1007/s00158-016-1495-1.

[77] Martins, J. R., and Lambe, A. B., "Multidisciplinary Design Optimization: A Survey of Architectures," *AIAA Journal*, Vol. 51, No. 9, 2013, pp. 2049–2075. https://doi.org/10.2514/1.j051895.

[78] Orndorff, N. C., and Hwang, J. T., "A Distributed Method for Solving Large-Scale Multidisciplinary Optimization Problems," *AIAA AVIATION FORUM AND ASCEND 2025*, AIAA, 2025. https://doi.org/10.2514/6.2025-3736.

[79] Wächter, A., and Biegler, L. T., "On the Implementation of an Interior-Point Filter Line-Search Algorithm for Large-Scale Nonlinear Programming," *Mathematical Programming*, Vol. 106, 2006, pp. 25–57. https://doi.org/10.1007/s10107-004-0559-y.

[80] Gill, P. E., Murray, W., and Saunders, M. A., "SNOPT: An SQP Algorithm for Large-Scale Constrained Optimization," *SIAM Review*, Vol. 47, No. 1, 2005, p. 99–131. https://doi.org/10.1137/s0036144504446096.

[81] Sarojini, D., Ruh, M., Yan, J., Scotzniovsky, L., Orndorff, N. C., Xiang, R., Zhao, H., Krokowski, J., Warner, M., van Schie, S., Cronk, A., Guibert, A. T., Chambers, J. T., Wolfe, L., Doring, R., Despins, R., Joseph, C., Anderson, R., Ning, A., Gill, H., Lee, S., Cheng, Z., Cao, Z., Mi, C., Meng, Y. S., Silva, C., Chen, J.-S., Kim, A. A., and Hwang, J. T., "Review of Computational Models for Large-Scale MDAO of Urban Air Mobility Concepts," *AIAA SCITECH 2024 Forum*, AIAA, 2024. https://doi.org/10.2514/6.2024-0377.

[82] Anderson Jr, J. D., *Fundamentals of Aerodynamics*, Tata McGraw-Hill Education, 2010.

[83] Katz, J., and Plotkin, A., *Low-Speed Aerodynamics*, Vol. 13, Cambridge University Press, 2001. https://doi.org/10.1017/cbo9780511810329.

[84] Ruh, M. L., and Hwang, J. T., "Robust Modeling and Optimal Design of Rotors Using Blade Element Momentum Theory," *AIAA AVIATION 2021 Forum*, AIAA, 2021, p. 2598. https://doi.org/10.2514/6.2021-2598.

[85] Ning, S. A., "A Simple Solution Method for the Blade Element Momentum Equations with Guaranteed Convergence," *Wind Energy*, Vol. 17, No. 9, 2014, pp. 1327–1345. https://doi.org/10.1002/we.1636.

[86] Pitt, D. M., and Peters, D. A., "Theoretical Prediction of Dynamic-Inflow Derivatives," *Sixth European Rotorcraft and Powered Lift Aircraft Forum*, 1980.

[87] Johnson, W., *Rotorcraft Aeromechanics*, Vol. 36, Cambridge University Press, 2013. https://doi.org/10.1017/cbo9781139235655.

[88] Drela, M., "XFOIL: An Analysis and Design System for Low Reynolds Number Airfoils," *Low Reynolds Number Aerodynamics: Proceedings of the Conference Notre Dame, Indiana, USA, 5–7 June 1989*, Springer, 1989, pp. 1–12. https://doi.org/10.1007/978-3-642-84010-4_1.

[89] Viterna, L. A., and Janetzke, D. C., "Theoretical and Experimental Power from Large Horizontal-Axis Wind Turbines," Tech. rep., NASA Lewis Research Center, Cleveland, OH (United States), 1982. https://doi.org/10.2172/6763041.

[90] Chauhan, S. S., and Martins, J. R., "Low-fidelity aerostructural optimization of aircraft wings with a simplified wingbox model using OpenAeroStruct," *EngOpt 2018 Proceedings of the 6th International Conference on Engineering Optimization*, Springer, 2019, pp. 418–431. https://doi.org/10.1007/978-3-319-97773-7_38.

[91] Sarojini, D., "Structural Analysis and Optimization of Aircraft Wings Through Dimensional Reduction," Ph.D. thesis, Georgia Institute of Technology, 2021.

[92] Young, W. C., Budynas, R. G., and Sadegh, A. M., *Roark's Formulas for Stress and Strain*, McGraw-Hill Education, 2012.

[93] Cesnik, C. E. S., and Hodges, D. H., "VABS: A New Concept for Composite Rotor Blade Cross-Sectional Modeling," *Journal of the American Helicopter Society*, Vol. 42, No. 1, 1997, p. 27–38. https://doi.org/10.4050/jahs.42.27.

[94] Lowson, M. V., and Ollerhead, J. B., "A Theoretical Study of Helicopter Rotor Noise," *Journal of Sound Vibration*, Vol. 9, No. 2, 1969, pp. 197–222. https://doi.org/10.1016/0022-460X(69)90028-5.

[95] Barry, F. W., and Magliozzi, B., "Noise Detectability Prediction Method for Low Tip Speed Propellers," Tech. Rep. AFAPL–TR–71–37, Air Force Aero Propulsion Laboratory, June 1971. https://doi.org/10.21236/ad0729432.

[96] Gutin, L., "On the Sound Field of a Rotating Propeller," Tech. Rep. NACA–TM–1195, National Advisory Committee for Aeronautics, 1936.

[97] Sears, W. R., and Sparks, B. O., "On the Reaction of an Elastic Wing to Vertical Gusts," *Journal of the Aeronautical Sciences*, Vol. 9, No. 2, 1941, pp. 64–81. https://doi.org/10.2514/8.10802.

[98] Kvurt, A., and Stalnov, O., "From the Blade Geometry to Prediction of Tonal Noise Component in Hover," *AIAA/CEAS Aeroacoustics Conference*, AIAA Paper 2022–3076, June 2022. https://doi.org/10.2514/6.2022-3076.

[99] Whelchel, J., Alexander, W. N., and Intaratep, N., "Propeller Noise in Confined Anechoic and Open Environments," *AIAA SciTech Forum*, AIAA Paper 2020–1252, Jan. 2020. https://doi.org/10.2514/6.2020-1252.

[100] Tinney, C., and Valdez, J., "Acoustic Scaling for Small Rotors in Hover," *Proceedings of the Vertical Flight Society 75th Annual Forum*, The Vertical Flight Society, Philadelphia, Pennsylvania, May 14–15, 2019. https://doi.org/10.4050/f-0075-2019-14457.

[101] Zawodny, N. S., Pettingill, N. A., Lopes, L. V., and Ingraham, D., "Experimental Validation of an Acoustically and Aerodynamically Optimized UAM Proprotor Part 1: Test Setup and Results," Tech. Rep. NASA–TM–20220015637, National Aeronautics and Space Administration, February 2023.

[102] Weatheritt, J., and Sandberg, R., "A Novel Evolutionary Algorithm Applied to Algebraic Modifications of the RANS Stress-Strain Relationship," *Journal of Computational Physics*, Vol. 325, 2016, pp. 22–37. https://doi.org/10.1016/j.jcp.2016.08.015.

[103] Fritsch, D. J., Vishwanathan, V., Roy, C. J., Lowe, K. T., Devenport, W. J., Croaker, P., Tkachenko, O., Pook, D., Lane, G., Shubham, S., and Sandberg, R. D., "Modeling the Surface Pressure Spectrum Beneath Turbulent Boundary Layers in Pressure Gradients," *AIAA Journal*, Vol. 61, No. 5, 2023, pp. 1–20. https://doi.org/10.2514/1.J062074.

[104] Lee, S., "Empirical Wall-Pressure Spectral Modeling for Zero and Adverse Pressure Gradient Flows," *AIAA Journal*, Vol. 56, No. 5, 2018, pp. 1818–1829. https://doi.org/10.2514/1.J056528.

[105] Lee, S., Ayton, L., Bertagnolio, F., Moreau, S., Chong, T. P., and Joseph, P., "Turbulent Boundary Layer Trailing-Edge Noise: Theory, Computation, Experiment, and Application," *Progress in Aerospace Sciences*, Vol. 126, Oct. 2021, p. 100737. https://doi.org/10.1016/j.paerosci.2021.100737.

[106] Li, S., and Lee, S., "Prediction of Rotorcraft Broadband Trailing-Edge Noise and Parameter Sensitivity Study," *Journal of the American Helicopter Society*, Vol. 65, No. 4, 2020, pp. 1–14. https://doi.org/10.4050/JAHS.65.042006.

[107] Brown, A., and Harris, W. L., "Vehicle Design and Optimization Model for Urban Air Mobility," *Journal of Aircraft*, Vol. 57, No. 6, 2020. https://doi.org/10.2514/1.C035756.

[108] Vegh, J. M., Botero, E., Clark, M., Smart, J., and Alonso, J. J., "Current Capabilities and Challenges of NDARC and SUAVE for eVTOL Aircraft Design and Analysis," *2019 AIAA/IEEE Electric Aircraft Technologies Symposium (EATS)*, 2019, pp. 1–19. https://doi.org/10.2514/6.2019-4505.

[109] Afonso, F., Ferreira, A., Ribeiro, I., Lau, F., and Suleman, A., "On The Design of Environmentally Sustainable Aircraft for Urban Air Mobility," *Transportation Research Part D: Transport and Environment*, Vol. 91, 2021, p. 102688. https://doi.org/https://doi.org/10.1016/j.trd.2020.102688.

[110] Cheng, Z., Zhao, S., Scotzniovsky, L., Rodriguez, G., Mi, C., and Hwang, J. T., "A Differentiable Method for Low-Fidelity Analysis of Permanent-Magnet Synchronous Motor," *AIAA SCITECH 2023 Forum*, 2023, p. 1091. https://doi.org/10.2514/6.2023-1091.

[111] Htwe, N. H. H., "Design of 50 kw Permanent Magnet Synchronous Motor for HEV," *Iconic Research and Engineering Journals*, Vol. 3, No. 2, 2019.

[112] Zhao, S. F., Huang, X. Y., Fang, Y. T., and Li, J., "A Control Scheme for a High Speed Railway Traction System Based on High Power PMSM," *2015 6th International Conference on Power Electronics Systems and Applications (PESA)*, 2015, pp. 1–8. https://doi.org/10.1109/PESA.2015.7398905.

[113] Lu, D., and Kar, N. C., "A Review of Flux-Weakening Control in Permanent Magnet Synchronous Machines," *2010 IEEE Vehicle Power and Propulsion Conference*, 2010, pp. 1–6. https://doi.org/10.1109/VPPC.2010.5728986.

[114] Etkin, B., *Dynamics of Atmospheric Flight*, Courier Corporation, 2005.

[115] Stevens, B. L., Lewis, F. L., and Johnson, E. N., *Aircraft Control and Simulation: Dynamics, Controls Design, and Autonomous Systems*, John Wiley & Sons, 2015. https://doi.org/10.1002/9781119174882.

[116] Silva, C., Johnson, W. R., Solis, E., Patterson, M. D., and Antcliff, K. R., "VTOL Urban Air Mobility Concept Vehicles for Technology Development," *2018 Aviation Technology, Integration, and Operations Conference*, 2018, p. 3847. https://doi.org/10.2514/6.2018-3847.

[117] van Schie, S. P., Ruh, M. L., Fletcher, A. H., Warner, M., Sperry, M., Scotzniovsky, L., Orndorff, N. C., Xiang, R., Yan, J., Zhao, H., Krokowski, J., Chen, J.-S., Sarojini, D., Gill, H., Lee, S., Tagg, A. C., Anderson, R., Green, E., Joseph, C., Ning, A., Cheng, Z., Cao, Z., Mi, C., Guibert, A. T., Cronk, A., Kim, A. A., Meng, S., Silva, C., and Hwang, J. T., "Large-Scale Distributed Multidisciplinary Design Optimization of the NASA Lift-Plus-Cruise Air Taxi Concept," *AIAA SCITECH 2025 Forum*, AIAA, 2025. https://doi.org/10.2514/6.2025-0362.

[118] Cheng, Z., Cao, Z., Mi, C., and Hwang, J. T., "Cost Optimization of Electric Vertical Takeoff and Landing Aircraft Through Powertrain Modeling," *Journal of Air Transportation*, Vol. 33, No. 3, 2025, p. 285–296. https://doi.org/10.2514/1.d0487.

[119] Yang, X.-G., Liu, T., Ge, S., Rountree, E., and Wang, C.-Y., "Challenges and Key Requirements of Batteries for Electric Vertical Takeoff and Landing Aircraft," *Joule*, Vol. 5, No. 7, 2021, p. 1644–1659. https://doi.org/10.1016/j.joule.2021.05.001.

[120] Jäger, F., Bertram, O., Lübbe, S. M., Bismark, A. H., Rosenberg, J., and Bartscht, L., "Battery-Electric Powertrain System Design for the HorizonUAM Multirotor Air Taxi Concept," *CEAS Aeronautical Journal*, Vol. 16, No. 3, 2024, p. 921–955. https://doi.org/10.1007/s13272-024-00759-1.

[121] Chapman, J. W., Tibor, S., and Camacho, T., "Thermal Management System Design for Electrified Aircraft Propulsion Concepts," *AIAA Propulsion and Energy Forum*, 2020. https://doi.org/10.2514/6.2020-3700.

[122] Brown, R., "Cheeseman Best Paper: Are eVTOL Aircraft Inherently More Susceptible to the Vortex Ring State than Conventional Helicopters?" *Proceedings of the Vertical Flight Society 79th Annual Forum*, The Vertical Flight Society, 2023, p. 1–17. https://doi.org/10.4050/f-0079-2023-18068.

[123] Ingraham, D., "Low-Noise Propeller Design with the Vortex Lattice Method and Gradient-Based Optimization," *AIAA SCITECH 2023 Forum*, AIAA, 2023. https://doi.org/10.2514/6.2023-2039.

[124] Böhnisch, N., Braun, C., Marzocca, P., and Muscarello, V., "Impact of Aerodynamic Interactions on Aeroelastic Stability of Wing-Propeller Systems," *Applied Sciences*, Vol. 14, No. 19, 2024, p. 8709. https://doi.org/10.3390/app14198709.

[125] Hoover, C. B., Shen, J., and Kreshock, A. R., "Propeller Whirl Flutter Stability and Its Influence on X-57 Aircraft Design," *Journal of Aircraft*, Vol. 55, No. 5, 2018, p. 2169–2175. https://doi.org/10.2514/1.c034950.